5-2014

Metal Chronometry for Pre-Detonation Nuclear Forensics Applications

Edward Thomas Peskie
University of Tennessee - Knoxville, epeskie@utk.edu

To the Graduate Council:

I am submitting herewith a thesis written by Edward Thomas Peskie entitled "Metal Chronometry for Pre-Detonation Nuclear Forensics Applications." I have examined the final electronic copy of this thesis for form and content and recommend that it be accepted in partial fulfillment of the requirements for the degree of Master of Science, with a major in Nuclear Engineering.

Howard L. Hall, Major Professor

We have read this thesis and recommend its acceptance:

Steven E. Skutnik, Maik K. Lang

Accepted for the Council:
Carolyn R. Hodges

Vice Provost and Dean of the Graduate School

(Original signatures are on file with official student records.)

5-2014

Metal Chronometry for Pre-Detonation Nuclear Forensics Applications

Edward Thomas Peskie
University of Tennessee - Knoxville, epeskie@utk.edu

To the Graduate Council:

I am submitting herewith a thesis written by Edward Thomas Peskie entitled "Metal Chronometry for Pre-Detonation Nuclear Forensics Applications." I have examined the final electronic copy of this thesis for form and content and recommend that it be accepted in partial fulfillment of the requirements for the degree of Master of Science, with a major in Nuclear Engineering.

Howard L. Hall, Major Professor

We have read this thesis and recommend its acceptance:

Steven E. Skutnik, Maik K. Lang

Accepted for the Council:
Carolyn R. Hodges

Vice Provost and Dean of the Graduate School

(Original signatures are on file with official student records.)

Metal Chronometry for Pre-Detonation Nuclear Forensics Applications

A Thesis Presented for the

Master of Science

Degree

The University of Tennessee, Knoxville

Edward Thomas Peskie

May 2014

Acknowledgements

I would like to thank my wife and daughter for their patience and my advisors for their guidance.

Abstract

The ability to determine the time since forming of seized nuclear material would provide crucial data to be used in its investigation. This paper examines the time dependent processes of diffusion; to include grain boundary diffusion, and discontinuous precipitation, and assess the utility of examination of impurity and alloying element concentration profiles, for use as a pre-detonation nuclear forensics tool for determining the age of a metal sample. Several examples provided illustrate the effects of time on both binary alloys and multi-component systems. This study draws parallels from studies of diffusion in mineral samples under geologic time and proposes modifications to that approach in order to determine the time since a metal sample was cast or formed. *PROFILER* software was used to generate concentration profiles. The second method involves calculating the number of damage sites caused self-irradiation during the α-decay of uranium isotopes. The OrigenARP module in SCALE 6.1 and SRIM-2008 were used to model the effects of these decays and predict the number of damage sites in an ideal sample. Further research is suggested to test the feasibility of combining the two approaches for forensic exploitation.

Table of Contents

List of Tables

List of Figures

Chapter 1

Introduction

Interdiction of a metallic component of nuclear material raises many questions of provenance, only some of which can be satisfactorily addressed today (1)(2)(3). For example, we can analyze for the date of last chemical purification by examining progeny isotopes. This proposed work will develop the means to answer another key question: when was the specimen cast or formed? We will do this through two approaches: 1) the examination of impurity diffusion in the microstructure of the metal and 2) the examination of internal radiolytic damage from self-irradiation.

An enhanced nuclear forensics capability that determines the materials critical parameters such as its timeline of processing would support investigations of seized illicit materials. Earlier casework has demonstrated that the significant information of investigational utility can be garnered not just from the nuclear materials, but also the containers, shields, and assorted other components of a seized illicit article (1). Notably, the first methodology we envision should be extensible for evaluation of the time since forming of any metallic sample, not just potential nuclear device components. The second methodology utilizes the chemical damage caused by radiolytic processes within the metal grain structure, which would be applicable specifically to radioactive metal systems, uranium in this case, but adaptable to other metal systems.

This is a new method of forensic interpretation that is not currently available to the nuclear materials forensics community. In the case of an interdicted sample, all forensics evidence that can be elucidated helps determine possible sources or pathways for the questioned object. Furthermore, the two approaches examined herein would be complementary for uranium metals and alloys, providing an additional cross-check on the results of each, and thus higher confidence in interpretive efforts. In principle, our proposed work is also applicable to metals broadly, including plutonium or other nuclear fuels, as well as uranium. In this analysis, however, the scope is limited to uranium for brevity.

1.1 Background

In the late 1970's, researchers from the Musee d'art et d'historie in Geneva and the Metropolitan Museum of Art in New York City collaborated on a project to investigate changes in the microstructure of silver-rich, Ag-Cu alloys at ambient temperatures, in an effort to explain the manner in which normally malleable, ductile silver becomes brittle. It has been well documented that ancient silver artifacts are found to be brittle after excavation, whether they appear to be corroded or display no external signs of corrosion.

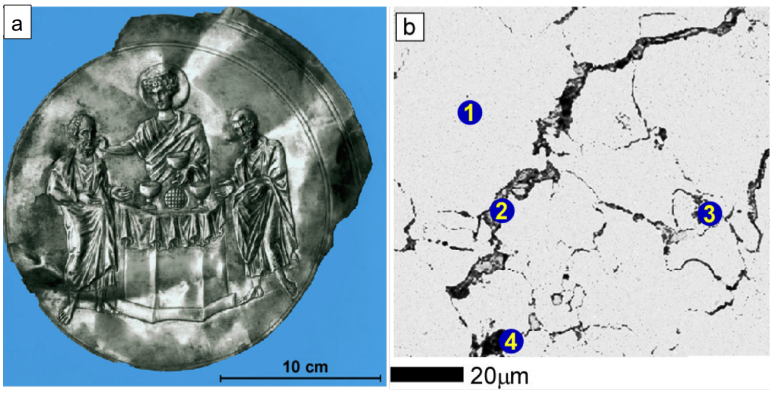

Figure 1.1: Examples of discontinuous precipitation in silver (4).

There are three primary causes for embrittlement in ancient silver. Corrosion-Induced Embrittlement occurs when alloys of high silver content undergo corrosion, which leads to brittle, finely granular surface layer of silver chloride (5). It is partly attributed to discontinuous cellular precipitation, the segregation of copper to grain boundaries, which occurs even at ambient temperatures (6).The manner of corrosion is localized galvanic attack. The moisture-containing, more noble metal acts as a cathode and the copper-enriched grain boundary region dissolves anodically (4). Microstructurally-induced embrittlement is characterized by brittle intergranular fracture, sharply defined cracks, and grain boundary facets, it is likely a consequence of long-term low temperature aging. Impurity elements segregate to grain boundaries, lead is believed to a significant contributor. Other elements, notably bismuth, can contribute in a co-segregating action with lead (5). Synergistic embrittlement is caused by corrosion along slip lines, grain boundaries and segregation bands that can result in cracks. The cracks then initiate fracture along embrittled grain boundaries under external loads. Grain boundary fractures expose more slip lines, grain boundaries and segregation bands to the environment, thereby increasing the opportunities for further corrosion (7).

Schweizer and Meyer (8) investigated discontinuous precipitation of copper in ancient silver alloys in an order to distinguish between copper that had precipitated rapidly at high temperatures and copper that had precipitated very slowly over many centuries. They based their conclusions on an observation that the interlamellar distance of a precipitated cell in silver alloys is a function of the temperature at which the precipitation occurred.

In order to apply this principle to the age verification of a sample, they generated an interlamellar distance versus temperature curve and sought to estimate the rate at which discontinuous precipitation occurred at room temperature, in the hopes of approximating the size of the precipitated cells in an ancient alloy that had been aging for several centuries. The curves used in their calculations are shown in Figure 1.2, where the vertical axis on the left indicates the growth rate of the reaction front in

microns per minute, such that the maximum growth rate at 25°C is 10^{-3} μm per year. Thus, a 1500 year-old sample should have precipitated cells of approximately 1.5 μm in diameter.

In 2003, R.J.H. Wanhill (4) compared the approximated values with samples taken from the Gundestrup Cauldron, the largest surviving silverwork from the European Iron Age, which dates from the 1st or 2nd centuries BC. The cauldron consists of twelve plates and a bowl, all of 95-98 percent silver. Chemical analysis has determined

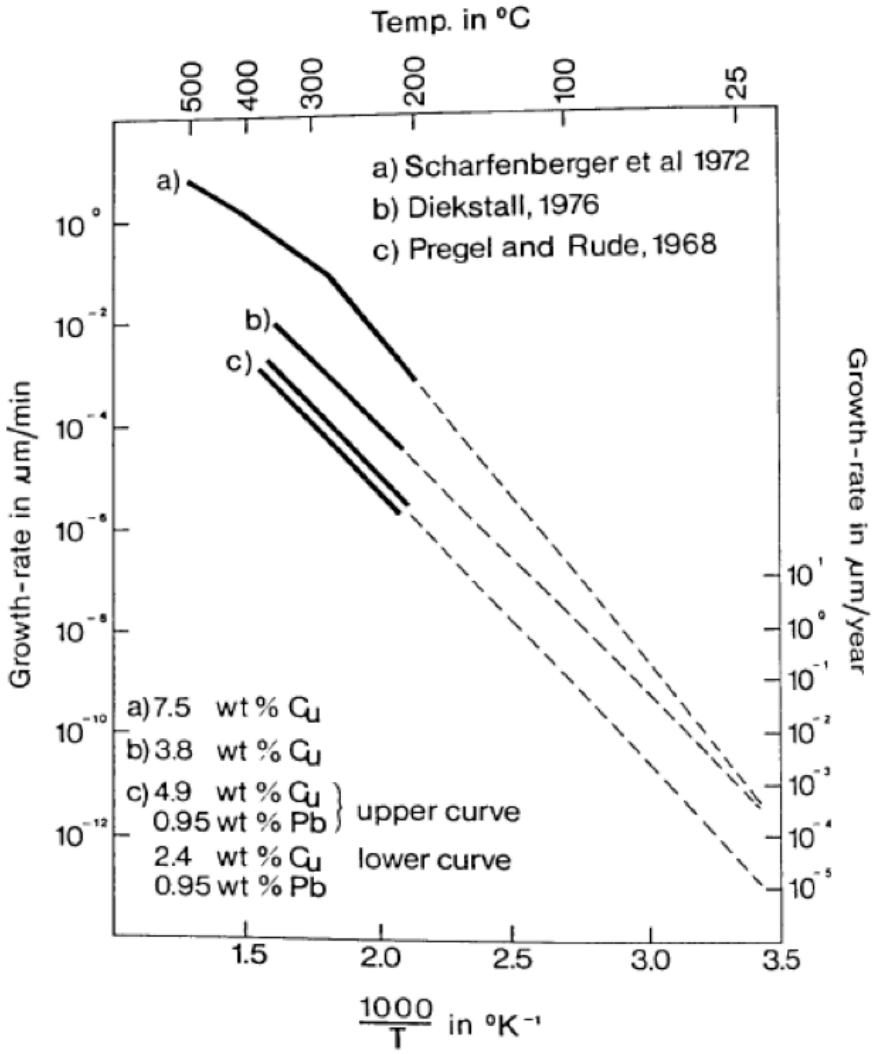

Figure 1.2: Curves showing the expected growth-rate of the discontinuous precipitation at ambient temperatures (8).

copper to be the main alloying (or impurity) element. It is relatively large, (50 cm in diameter), and due to its high quality workmanship, the cauldron has been the subject of numerous studies. He examined the samples using a Field Emission Gun Scanning Electron Microscope (FEG-SEM) and automated Electron BackScatter Diffraction (EBSD) equipment. Samples from the cauldron contained precipitate widths up to 7 μm, well beyond the predicted maximum of 2.1 to 2.2 μm, thus ruling out the use of precipitate widths for authentication. Furthermore, evidence (9) indicates that the copper precipitate is not lamellar and presents a mottled appearance, eliminating the notion that interlamellar distances could be used to authenticate a sample (7). A non-uniform growth of DP colonies from different boundaries in the same microstructure is frequently observed in the experimental studies for the following reasons: the physical orientation between the GB and the precipitate habit planes, and the dynamic properties of grain and interphase boundaries are dependent on their structure and can vary widely in a polycrystalline aggregate (10).

Chapter 2

Diffusion

2.1 Fundamentals

Diffusion in solids occurs on microscopic scales through the motion of discrete entities (atoms, molecules, clusters and lattice vacancies). These motions are the result of a statistical distribution of kinetic and potential energy expected among the atoms (11). The process is the thermally-activated, relative movement (flux) of atoms or molecules that is a response to forces such as gradients in chemical potential or temperature. The process is spontaneous, and must result in a net decrease in free energy (12). As an example, consider the movement of Δn_i moles of component i from region (II) of a higher chemical potential (μ_i^{II}) to a region (I) of lower chemical potential (μ_i^{I}). This motion will cause the total Gibbs energy (G) of the system to fall according to the following relationship:

$$\Delta G^I + \Delta G^{II} = \Delta n_i \left(\frac{\partial G^I}{\partial n_i} \right)_{P,T,n_j} - \Delta n_i \left(\frac{\partial G^{II}}{\partial n_i} \right)_{P,T,n_j} \tag{2.1}$$

when applying the definition of μ_i^I:

$$\Delta G^{Total} = \Delta n_i (\mu_i^I - \mu_i^{II}) < 0 \tag{2.2}$$

Thus, the chemical potential gradient generates the thermodynamic force necessary to cause atomic movement. Linear equations are sufficient for relating fluxes on the macroscopic level, however since each component of a system may be influenced by the gradient in chemical potential of any other component, diffusion in multicomponent systems becomes increasingly more complex.

2.1.1 Fick's Laws

In the presence of a concentration gradient, more impurity atoms will jump in the direction of the gradient than opposite it, creating a flux of diffusing atoms. Fick's first law governs this interaction; stating that the flux F per unit area per unit time is proportional to the diffusion coefficient and the one-dimensional concentration gradient.

$$F = -D\frac{dC}{dx} \tag{2.3}$$

where C is the dopant concentration per unit volume. The diffusion coefficient D depends on the individual type of atom and is strongly temperature dependent, defined by

$$D = -D_0 exp\left(\frac{-E_a}{kT}\right) \tag{2.4}$$

where D_0 is the diffusion coefficient extrapolated to infinite temperature, in units of m^2/s and E_a is the activation energy in eV. The motion of a diffusant is determined by a combination of a material's crystallography, its intermolecular forces and defects. The diffusion mechanism is also dependent on factors such as the size of the diffusing atom compared to the host lattice atoms and whether or not a defect-assisted process is required.

If an interstitial atom is small enough, when compared to atoms of the host lattice, it can jump from one interstitial site to another rather freely. Figure 2.1 compares bulk diffusion data for several impurity elements (13) in uranium extrapolated to

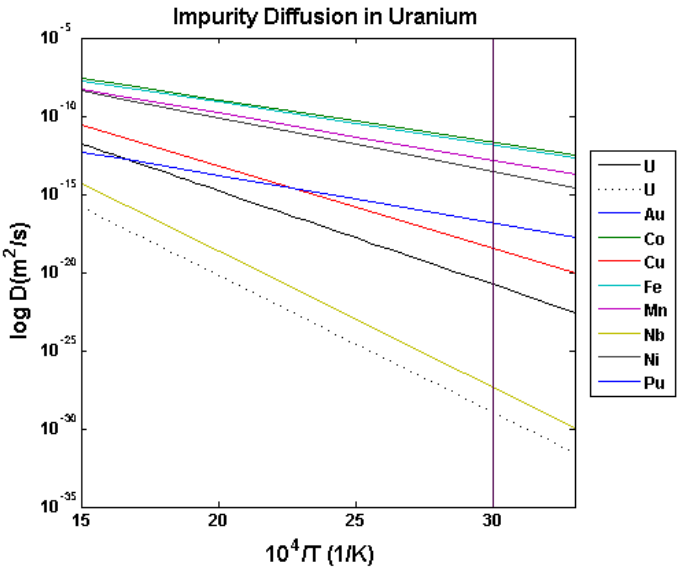

Figure 2.1: Diffusion of several interstitial solutes in U. U self-diffusion is shown for comparison.

ambient temperatures. Interstitial diffusers have much smaller activation enthalpies than those for self-diffusion.

Unless the experiment attains a steady state, time is also a variable, and a continuity equation must be solved. Diffusion's time dependence is governed by Fick's second law:

$$\frac{\partial C}{\partial t} = \frac{\partial}{\partial x}\left[D\frac{dC}{dx}\right] \tag{2.5}$$

This equation considers the time dependence of the diffusion process. However when D is independent of concentration C, and not a function of position (x) this equation simplifies to

$$\frac{\partial C}{\partial t} = D\left(\frac{\partial^2 C}{\partial x^2}\right) \tag{2.6}$$

By applying the chain rule to Fick's second law (Equation 2.5), a system of n components in a volume of fixed reference is expressed a follows:

$$\begin{aligned} F_1 &= -D_{11}\left(\frac{\partial C_1}{\partial x}\right) - D_{12}\left(\frac{\partial C_2}{\partial x}\right) \ldots\ldots\ldots\ldots\ldots\ldots D_{1(n-1)}\left(\frac{\partial C_{n-1}}{\partial x}\right) \\ F_2 &= -D_{21}\left(\frac{\partial C_1}{\partial x}\right) - D_{22}\left(\frac{\partial C_2}{\partial x}\right) \ldots\ldots\ldots\ldots\ldots\ldots D_{2(n-1)}\left(\frac{\partial C_{n-1}}{\partial x}\right) \\ F_{n-1} &= -D_{(n-1)}\left(\frac{\partial C_1}{\partial x}\right) - D_{(n-1)2}\left(\frac{\partial C_2}{\partial x}\right) \ldots\ldots\ldots D_{(n-1)(n-1)}\left(\frac{\partial C_{n-1}}{\partial x}\right) \end{aligned} \tag{2.7}$$

Using matrix multiplication, Equation 2.7 can be rewritten as:

$$\begin{bmatrix} J_1 \\ J_2 \\ \ldots \\ J_{n-1} \end{bmatrix} = - \begin{bmatrix} D_{11} & D_{12} & \ldots & D_{1(n-1)} \\ D_{21} & D_{22} & \ldots & D_{2(n-1)} \\ \ldots\ldots\ldots & & & \\ D_{(n-1)1} & \ldots\ldots & \ldots & D_{(n-1)(n-1)} \end{bmatrix} \begin{bmatrix} \partial C_1/\partial x \\ \partial C_2/\partial x \\ \ldots \\ \partial C_{(n-1)}/\partial x \end{bmatrix} \tag{2.8}$$

or simply as

$$\boldsymbol{J} = -\boldsymbol{D}\frac{\partial \boldsymbol{C}}{\partial x} \tag{2.9}$$

so that:

$$\frac{\partial \boldsymbol{C}}{\partial t} = \frac{\partial}{\partial x}\left(\boldsymbol{D}\frac{\partial \boldsymbol{C}}{\partial x}\right) \tag{2.10}$$

where $\boldsymbol{J}$ and $\boldsymbol{C}$ are column vectors and $\boldsymbol{D}$ is a matrix of diffusion coefficients. The $\boldsymbol{D}$ matrix must always have real, positive eigenvalues, which constrains the values of the elements within the matrix (14). Often, due to a lack of experimental data, the off-diagonal terms are neglected, and we are forced to assume (at some risk) that they are zero. If $n = 2$, then Equations 2.7 and 2.9 reduce to the binary diffusion flux, where D_{11} is the binary interdiffusion coefficient. The $\boldsymbol{D}$ matrix is usually *not* symmetrical, however it can be related to two symmetric matrices, $\boldsymbol{L}$ and $\boldsymbol{G}$ as follows:

$$\boldsymbol{D} = \boldsymbol{L}\boldsymbol{G} \tag{2.11}$$

Where the $\boldsymbol{L}$ matrix is the Onsager matrix of kinetic or phenomenological coefficeints, and $\boldsymbol{G}$ is the thermodynamic matrix. Both matrices have real, positive eigenvalues, and as such, the $\boldsymbol{D}$ matrix must meet those conditions.

2.1.2 Grain Boundary Diffusion

Grain boundary (GB) diffusion controls discontinuous precipitation (DP) reactions, and represents atomic transport due to the random displacement of atoms along GBs. It is known to have the smallest activation energy within bulk transport mechanisms and as such, occurs several orders of magnitude faster than diffusion in the bulk material. GB thickness, orientation, the proportion of solute atoms and the saturation level of the GB all affect GB diffusion (15). The grain boundary diffusivities for DP can be evaluated using the Petermann-Hornbogen equation:

$$s\delta D_{gb} = \frac{RT}{-8\Delta G}\lambda\nu \tag{2.12}$$

where D_{gb} is the grain boundary diffusion coefficient, δ is the grain boundary width, s is the segregation factor, ν is the velocity for the process, ΔG is the total driving force in terms of the overall change in the Gibbs energy, R is the gas constant, T is the absolute temperature of the process, and λ is the interlamellar spacing. The overall change in Gibbs energy contains both a chemical and interfacial component. The term $s\delta D_{gb}$ is known as the grain boundary diffusivity triple product and can be experimentally determined by measuring the parameters ν and λ. In 1998, Zieba and Gust (16) observed variations in the values of $s\delta D_{gb}$ by a factor of 10 when comparing various colonies in the same material, and attributed this variation to grain boundary properties such as misorientation of neighboring grains and the inclination of the grain boundary plane. In order to diminish or eliminate existing discrepancies in measurements, they applied a local approach to DP kinetics in Ni-4 at.% Sn and Al-22 at.% Zn (17). The local approach is based on the assumptions that each colony and potentially even each set of lamellae migrate at their own velocity, and thus the

solute concentration profile and the thickness of each lamellae change from lamella to lamella. This approach requires analytical electron microscopy to determine the solute distribution behind mobile reaction fronts. Through a local approach, measuring the concentration profile of the solute and combining it with the value for lamellae thickness and growth rate, one can calculate the grain boundary diffusion coefficient using the diffusion model of the DP reaction shown in Equation 2.13, as proposed by Cahn (18).

$$x(y) = (x_e - x_0)\frac{\cosh((y-0.5)\sqrt{C})}{\cosh(\frac{\sqrt{C}}{2})} + x_0 \tag{2.13}$$

Where the diffusivity at the migrating GB is related to the Cahn parameter (C), by Equation 2.14.

$$C = \frac{\nu_{in}\lambda_\alpha^2}{s\delta D_{gb}} \tag{2.14}$$

In these equations, y is a coordinate measured perpendicularly from the edge of the β lamella to the α lamella, x_0 is the solute concentration of the alloy, ν_{in} is the instantaneous velocity of the reaction front, λ_α is the local value of the a phase lamellar thickness, and the GB diffusivity triple product is as defined in Equation 1. After evaluating local values of diffusivity in the following alloys, Al–Zn, Ni–Sn, Cu–In and Co–Al, they drew the following conclusion: there is no significant difference in the rate of diffusion along stationary and migrating GBs in such systems as Al–Zn, Ni–Sn and Cu–In.

Manna et al. (10) illustrated that DP can be completely suppressed by the deactivation of an otherwise suitable initiation site in Cu-–In. After 100 hours of aging at 423 K, the surfaces of a Cu-7.5 at.% In crystal showed no signs of DP. The suppression was attributed to deactivation of the nucleation site by forming a synthetic In–rich intermetallic-alloyed zone that is not capable of undergoing the thermally activated migration and initiation of DP.

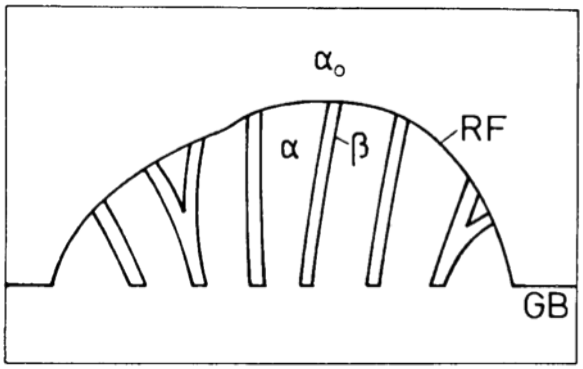

Figure 2.2: Schematic representation of discontinuous precipitation occurring at grain boundary (GB) and growing behind a migrating reaction front (RF) advancing to a supersaturated α_0 grain (10).

2.2 Discontinuous Precipitation

Discontinuous precipitation is a solid-state phase transformation, (see Figure 2.2) in which a supersaturated solution, α_0, decomposes in equilibrium α+β phases. The transformation initiates at heterogeneous sites, often grain boundaries. The newly formed phases grow cooperatively into the surrounding α_0 grains. The reaction often competes with a homogeneous precipitation process inside the α_0 matrix, which is sometimes called continuous precipitation (CP). DP is generally regarded as undesirable because it deteriorates the strength of GBs, and suppresses CP, often inducing precipitation hardening. The microstructure of DP aggregates behind migrating reaction fronts exhibit a cellular morphology similar to those seen in eutectoid decomposition, such as pearlites in steels. They normally display a lamellar morphology, but can also exhibit fibrous, rod-like or globular morphologies. To date, a number of alloys have been investigated (19). Many discontinuous reactions occur by initially exhausting available nucleation sites (GBs), and a subsequent growth stage where no further nucleation occurs (20).

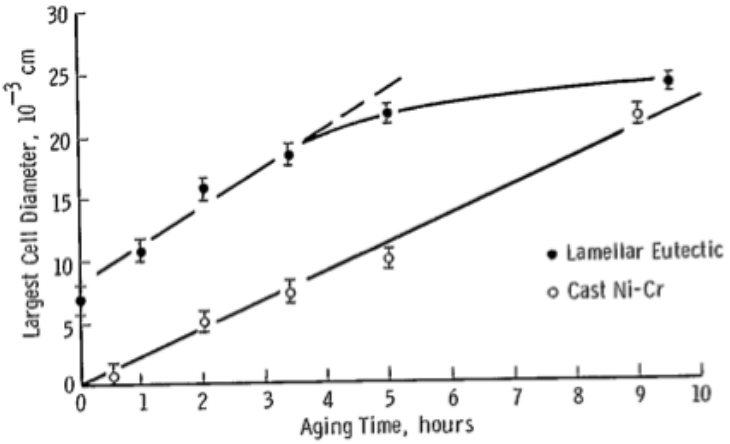

Figure 2.3: Largest cell size as a function of aging time at 760°C Nickel alloys (21).

2.2.1 Binary Alloys

DP has been investigated in nickel-chromium alloys, and determined that cellular growth begins at grain boundaries or other defects and leaves behind a lamellar structure. The precipitate's direction of growth is determined by the local orientation of the grain boundaries. Kossowsky (21) determined that the linear growth rate is obtained from the slope of a line in a plot of the largest cell diameter versus aging time (see Figure 2.3). In the cast alloy, the line extrapolated to zero at an aging time of zero, as expected. In the eutectic alloy, zero aging time corresponds to a cell diameter of 75 μm, the largest of the existing cells. As time increased, larger precipitates were formed, presumably growing from the preexisting cells. In a 1972 study measuring DP in aluminum-based zinc alloys, Malhotra (20) established a linear relationship between time and the thickness of the precipitates. He employed two methods for measuring the average growth rate. The first, Equation 2.15, uses a simultaneous measurement of X, the volume fraction transformed, and S_v, the surface area per unit volume of the advancing interface, using the relation:

$$\bar{G} = \frac{dX}{dt} * \frac{1}{S_v} \tag{2.15}$$

where dX/dt is the slope of the X vs t plot at the time of interest. The second method used the Turnbull model, which predicts constant lamellar spacing and growth rate according to Equation 2.16:

$$G = \frac{4\delta D_{gb}}{S^2} \tag{2.16}$$

where G is the lamellar growth rate, D_{gb} is the solute diffusivity along the cell boundary, S is lamellar spacing, and δ is the cell boundary thickness. Using a grain boundary diffusion coefficient based on an estimate for pure zinc, applied to Equation 2.16, yielded a growth rate very close to that obtained experimentally, and reinforced boundary diffusion as a controlling factor in discontinuous precipitation reactions. Also of note, the addition of tin to the alloy served to impede diffusion. Tin atoms trapped vacancies, thereby slowing the diffusion rate of the advancing interface, reducing the precipitates growth rate. Figure 2.4 shows the dependence of lamellar spacing, S, on discontinuous precipitation as a function of temperature. The lamellar structure nucleates at GBs and grows perpendicularly to them. It stops only if the volume fraction of continuous precipitation is significant to impede its growth. Lamellar spacing is defined as Equation 2.17, by the Turnbull theory for cell growth.

$$S = \frac{-4\gamma V}{\Delta G} \tag{2.17}$$

Where γ is the interfacial energy, V the molar volume, and ΔG is the free energy associated with the cellular reaction. Lower temperatures correspond to shorter interlamellar spacing, and that spacing remains constant with increases in aging time for all temperatures.

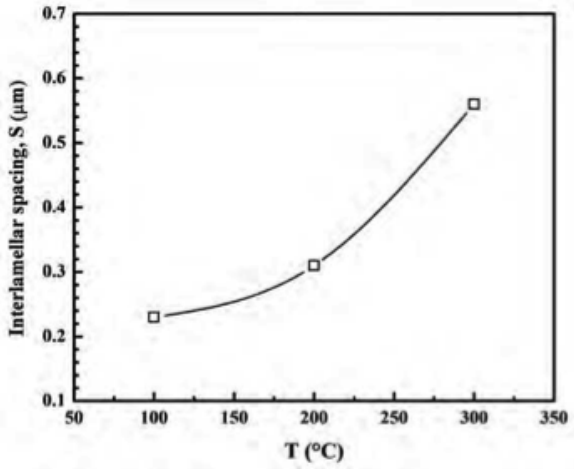

Figure 2.4: Interlamellar spacing as a function of aging temperature in a Mg-Zn-Al alloy (20).

2.2.2 Multicomponent Systems

Diffusion in multi-component systems involves the simultaneous flow of more than two components. In these systems, the flux of each component is dependent upon its own concentration and chemical gradient and that of all other diffusing components.

Cellular precipitation does not always occur in multi-component systems such as steel, where the material contains interstitial and substitutional solutes with widely different diffusivities. More importantly, the growth features typically observed during cellular precipitation in binary substitutional systems are not present in multicomponent systems. The composition of alloys can impede or promote DP during annealing. Saucedo et al.(22) examined precipitation in steel alloys and found agreement between experimental results and theory that steels with the highest concentration of interstitial solutes (C and N) had the highest kinetics of precipitation, and volume fraction of precipitation, while steels with the highest concentration of Mn allowed only carbides to precipitate, as Mn maintains N in the solid solution.

In 1991 Kikuchi et al. (23) published a comprehensive review of cellular precipitation in Cr–Ni austenitic steels. Cellular precipitation of $Mn_{23}C_6$ or Cr_2N

often occurs when nitrogen is alloyed to Cr–Ni or Cr–Mn austenitic stainless steels. Adding nitrogen to high chromium austenitic alloys enhances the cellular precipitation of $Mn_{23}C_6$, and when no carbon is used in nitrogen alloyed Cr–Ni and Cr–Mn steels, the dominant precipitate is Cr_2N. Typically, DP stops in these systems once cells cover 80-90% of the grains, unlike the constant growth rates seen in binary substitutional alloys.

In 2010, Contreras-Piedras et al. (24) examined microstructural evolution and growth kinetics in a magnesium alloy. They sought evidence of grain boundary diffusion and to evaluate the effects of temperature on cellular spacing. Figure 2.5 shows the volume fraction of cellular precipitation vs. aging time. The lowest aging temperature yielded the highest volume fraction. The analysis of the plot was done using the Johnson-Mehl-Avrami-Kolmogorov equation, which governs most discontinuous phase transformations:

$$X_f = 1 - e^{-kt^n} \tag{2.18}$$

Where X_f is the volume fraction transformed, t is time, and k and n are constants whose values depend on the nucleation and growth rate of the transformation product. An n value of 1 corresponds to a boundary, and values obtained experimentally were 1.1, 0.85 and 0.87 for 100, 200 and 300°C, respectively. Cellular spacing increased with aging time, in accordance with the Turnbull theory and the activation energy indicated a grain boundary diffusion process. Figure 2.6 compares the volume fraction of the cell, V_v, versus reaction time in four 25Cr-20Ni steels with varying nitrogen concentrations aged at 1073 K. While the incubation time decreased as the nitrogen content increased, cellular precipitation was complete after 100 h, independent of the nitrogen concentration, suggesting that the migration rate of the cell boundary decreases with increasing reaction time.

The non-steady state growth of precipitates can be qualitatively explained by three factors. The first is the transfer of the faster diffusing element, nitrogen. At

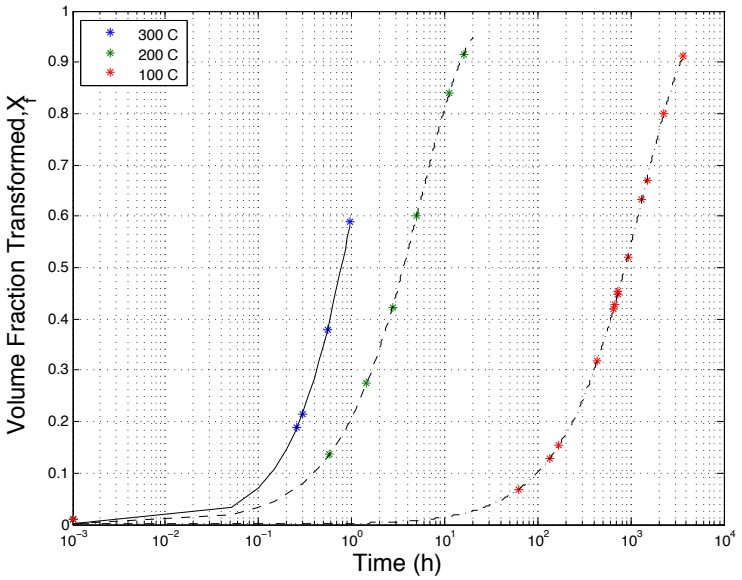

Figure 2.5: Volume fraction of cellular precipitation vs. aging time of the alloy aged at 100, 200, and 300°C (22).

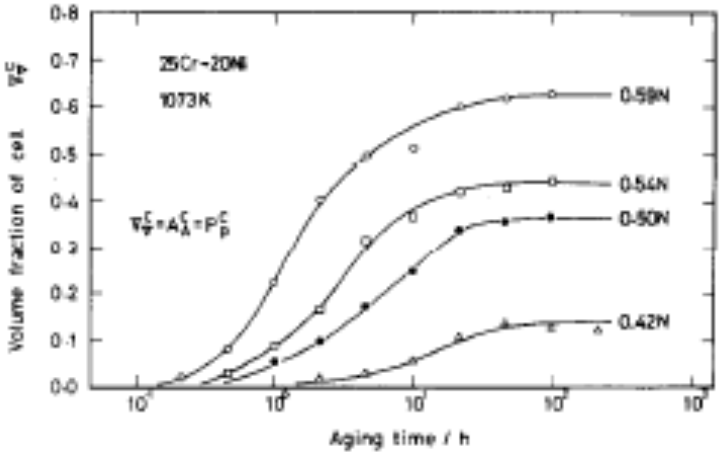

Figure 2.6: Change in the volume fraction of cellular precipitate with reaction time at 1073 K (23).

1073 K, the volume diffusion coefficient of nitrogen in Cr–Ni austenitic stainless steel is five orders of magnitude larger than that of chromium (23). Initially, the boundary diffusion of chromium is the rate-controlling factor. However, as the reaction progresses, the growth rate as defined in Equation 2.16, becomes larger than observed growth rate. The difference between the experimentally observed growth rate and the growth rate governed by volume diffusion (Equation 2.19) decreased by an order of magnitude. This is primarily attributed to the interlamellar spacings inability to increase rapidly enough to match the decreasing migration rate of the moving cell boundary. This suggests that the volume diffusion of chromium may have increased significance in the later stages of cellular precipitation.

$$G = \frac{D_\nu}{S} \tag{2.19}$$

The second factor is the deceleration of the moving cell boundary. Nitrogen supersaturation in the untransformed matrix is the driving force for the precipitation of Cr_2N in Cr–Ni austenitic steel. Once precipitation begins, nitrogen, the faster-diffusing element flows from the untransformed matrix to the cell via long-range diffusion. This action decreases the amount of nitrogen in the untransformed matrix, which in turn, decreases the migration rate of the moving cell boundary. The final factor is the stoppage of cell boundary movement. Under steady-state conditions where the growth rate is constant, a diffusion zone exists ahead of a moving cell boundary. Its width is defined by the growth rate divided by the volume diffusivity. As the migration rate decreases, the diffusion zones width increases, and is accompanied by a loss in chemical diving force for cellular precipitation. This causes a continued decrease in the migration rate until it eventually stops. In 2004, Santhi-Srinivas and Kutumbarao (25) studied DP a multi-component (Fe–Cr–Mn–N) system. Of note, for temperatures below 700°C, they observed no DP. And for temperatures above 700°C, they found that the volume fraction and precipitate cell size increased sigmoidally with time, in agreement with the results shown in Figures 2.5 and 2.6. Based on

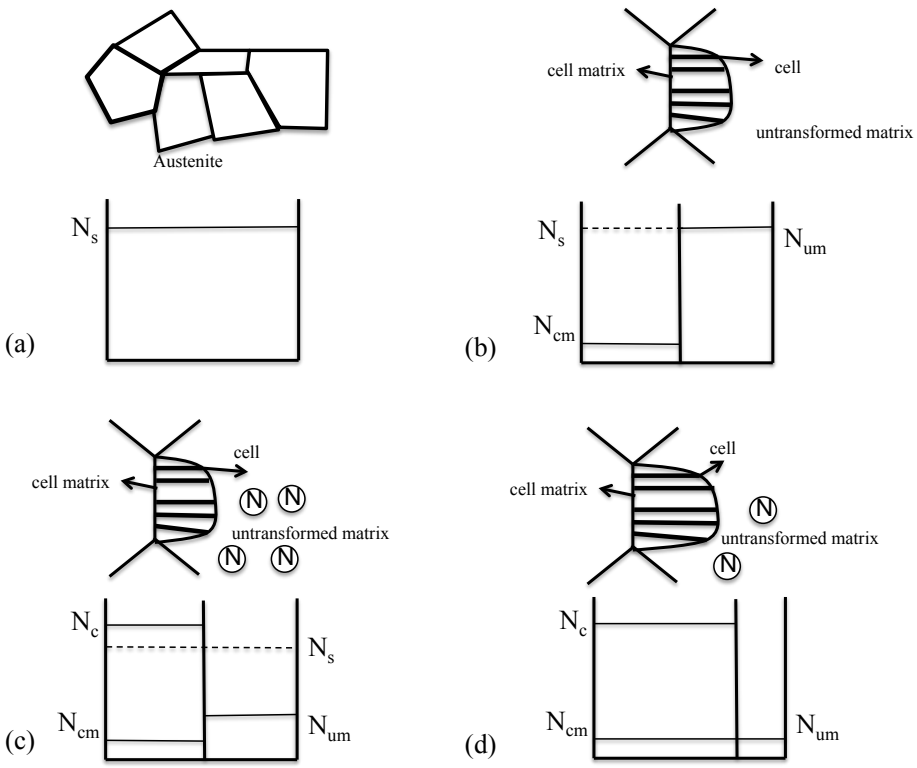

Figure 2.7: Growth mechanism for DP in the multi-component system (Fe-Cr-Mn-N). (a) nitrogen concentration in solution-treated samples; (b) formation of cells after aging at t=t_1; (c) nitrogen diffusion at t=t_2;(d) termination of cell growth at t=t_3 (25).

their observations and the work of Kikuchi, they proposed a six-step description of the growth mechanism for DP in multicomponent systems. The mechanism outlined in Figure 2.7 can be described as follows:

1. In the solution treated sample, the concentration of nitrogen is uniform and is represented by N_s in Figure 2.7(a).

2. After aging, Cr_2N lamellae form by absorbing nitrogen from the immediate surrounding matrix, which becomes highly depleted of nitrogen. The concentration of nitrogen in the cell matrix (N_{cm}) decreases with the formation of lamellae

while the concentration of nitrogen in the untransformed matrix N_{um} remains the same as N_s, as shown in Figure 2.7(b).

3. This process creates a large concentration gradient between the untransformed matrix and the cell matrix, which results in the flow of nitrogen to the cell matrix.

4. Long-range diffusion of nitrogen from the untransformed matrix is needed for the growth of Cr_2N lamellae. Figure 2.7(c)

5. As aging continues, the concentration of nitrogen in the untransformed matrix (N_{um}) decreases and nitrogen concentration in the cell (N_c) increases as more nitrogen diffuses to cause growth. As the gradient between the untransformed matrix and the cell continuously decreases, the diffusion rate of nitrogen and hence the migration rate of the cell boundary decreases with reaction time.

6. As aging progresses, N_{um} decreases further. Eventually, when chemical equilibrium is reached, (N_{um}=N_{cm}), as shown in Figure 2.7(d), cell growth stops, leading to an incomplete cellular reaction.

This six-step process differs from the method proposed by Kikuchi in three ways: long-range diffusion of nitrogen was assumed to take place from the untransformed matrix to the cell; the observed concentration of chromium in the untransformed matrix did not change (emphasis was placed on the volume diffusion of nitrogen and corresponding decrease in the migration rate of the cell boundary), and finally, boundary migration and cell growth were assumed to stop when the cell matrix and the untransformed matrix reached chemical equilibrium.

Chapter 3

Modeling

3.1 Diffusion-Assumptions

Complex diffusion processes in multicomponent alloys are often not analytically solved, and must be dealt with numerically. In order to simplify these calculations, a key assumption is possible to alleviate the need for extensive calculations. The analysis of multi-component diffusion can be simplified by utilizing the concept of effective binary diffusion coefficient (EBDC), treating an alloy as if there are only two components, a solute and a solvent matrix.

3.1.1 Effective Binary Diffusion Coeffcient (EBDC)

The system in Equation 2.7 required $n-1$ flux equations in a system of n components. The diagonal terms illustrate the effects of a component's concentration gradient on its flux, and the off-diagonal terms illustrate the ability of the remaining components to influence the flux. The system of equations in Equation 2.7 can be simplified to:

$$J_1 = -D_1(EB)\frac{\partial C_1}{\partial x} \tag{3.1}$$

as if there were only two components. $D_1(EB)$ represents the effective boundary diffusion coefficient of component 1. $D_1(EB)$ is different for each component, which is not the case in true binary diffusion. If we are to model the diffusion couple as semi-infinite, such that initial concentrations are preserved at sufficiently large distances from the interface ($x = 0$), and that no concentration gradient exists on either side of the couple, we must also assume that the EBDC of a component is independent of distance within the diffusion zone. The solution to the isothermal diffusion equation is as follows (14)(26):

$$C_i(t,x) = C_i(0) + \frac{\Delta C^0}{2}\left[1 - erf\left(\frac{x}{2\sqrt{D_{i(EB)}t}}\right)\right] \tag{3.2}$$

where ΔC^0 is the initial difference between the concentrations of the components on each side of the couple, $C_i(0)$ is the lower of the two initial values of C_i. Calculation of an EBDC requires knowledge of the self-diffusion coefficients of all the diffusing components and the concentration gradients of all but one component. Extensive, current diffusion data can be found in Neumann's *Handbook of Experimental Data* (13).

3.1.2 Influence of Time and Temperature

Using Figure 3.1(b), Ganguly (27) determined that the true value of Dt is related to the calculated value $[(Dt)_c]$ from the measured concentration profile by the relationship:

$$Dt = (Dt)_c - \frac{\epsilon^2}{2} \tag{3.3}$$

where ϵ is the standard deviation of the distribution of intensities of X-rays from the spatial averaging of the microprobe beam. A diffusion profile clearly exists in Figure 3.1(a). However the data points for the Mn-profile are too irregular to be of help in the analysis, and the Ca and Fe profiles were used in the determination of

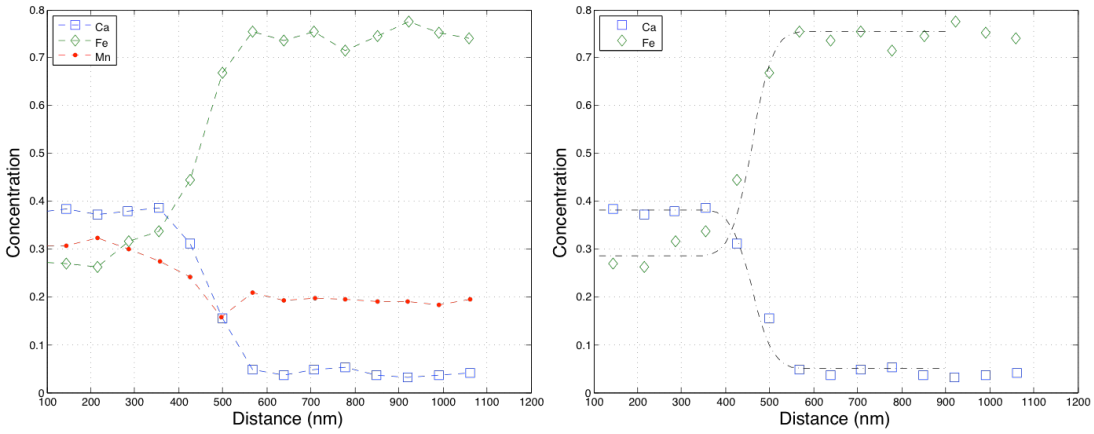

Figure 3.1: (a) Concentration profile of divalent cations. (b) Fits of measured conentration profiles in ATEM of Ca (squares) and Fe (triangles) across the overgrowth interface with Dt=7.5x10^{-12} cm^2(27).

Dt. The best fit for the data in Figure 3.1(b) using multicomponent diffusion values is given by Dt=7.5x10^{-12} cm^2. This value was within the acceptable range inferred from the deconvolution of profiles by electron microprobe. The Dt values for each diffusant need not be the same, as the values for Ca and Fe could differ from each other, however in this case, the calculated data supported experimental results in which the EBDCs of Fe and Ca have been found to be essentially the same (27).

Diffusion is a function of time due to its dependence on temperature. Ganguly (27) investigated the application of the value of Γ (Equation 3.4) to determine the time scale of effective diffusion during regional metaomorphism in minerals, a natural garnet-garnet diffusion couple. Nonisothermal diffusion can be reduced to an isothermal diffusion problem (through the period of effective diffusion) by determining the characteristic temperature T_{Ch} as follows:

$$\int_{t_0}^{t'} D(t)dt = D(T_{Ch})(t' - t_0) = \Gamma \tag{3.4}$$

By increasing the number of isothermal steps, one can improve accuracy in calculations. Similarly, one can determine a characteristic diffusion coefficient based off the characteristic temperature in Equation 3.4 (28)(26). Using the value of Dt=7.5x10^{-12} cm^2, and solving Equation 3.4 for Δt yields:

$$\Delta t = \frac{7.51 * 10^{-12} cm^2}{D_{i(EB)}(T_{Ch})} \tag{3.5}$$

where $\Delta = t' - t_0$ and $D_{i(EB)}(T_{Ch})$ is the effective binary diffusion coefficient at the characteristic temperature. As outlined in Section 3.1.1, in order to calculate the EBDC for a component, one must know that self-diffusion coefficients for all the diffusing components, and the concentration gradients of $n-1$ components. Also, as in the case of the Mn profile in Ganguly's geological example, (27) one can eliminate diffusing components with poorly defined profiles that would otherwise distort or complicate the solution, however, in a forensics application, using as many components as possible would aid in the improving accuracy. Similarly, to average the EBDC of components within the diffusion zone, one can assume a constant $D_{i(EB)}$ and use values from the center of the diffusion zone, as shown in Figure 3.1(b). In order to determine the EBDC for diffusion in a semi-infinite couple we see that:

$$D_{Fe(EB)} = D_{FeFe} + D_{FeCa}\frac{\partial C_{Ca}}{\partial C_{Fe}} \tag{3.6}$$

$$D_{Ca(EB)} = D_{CaCa} + D_{CaFe}\frac{\partial C_{Fe}}{\partial C_{Ca}} \tag{3.7}$$

It is at this point, that the method for geological mixtures varies from that of metal alloy diffusion. In order to populate the $\boldsymbol{D}$ matrix, Ganguly used the following equation for thermodynamically ideal solutions:

$$D_{ij} = D_i^* \delta_{ij} - \frac{(X_i D_i^*)(D_j^* - D_n^*)}{\sum_{i=1}^{n} X_i D_i^*} \tag{3.8}$$

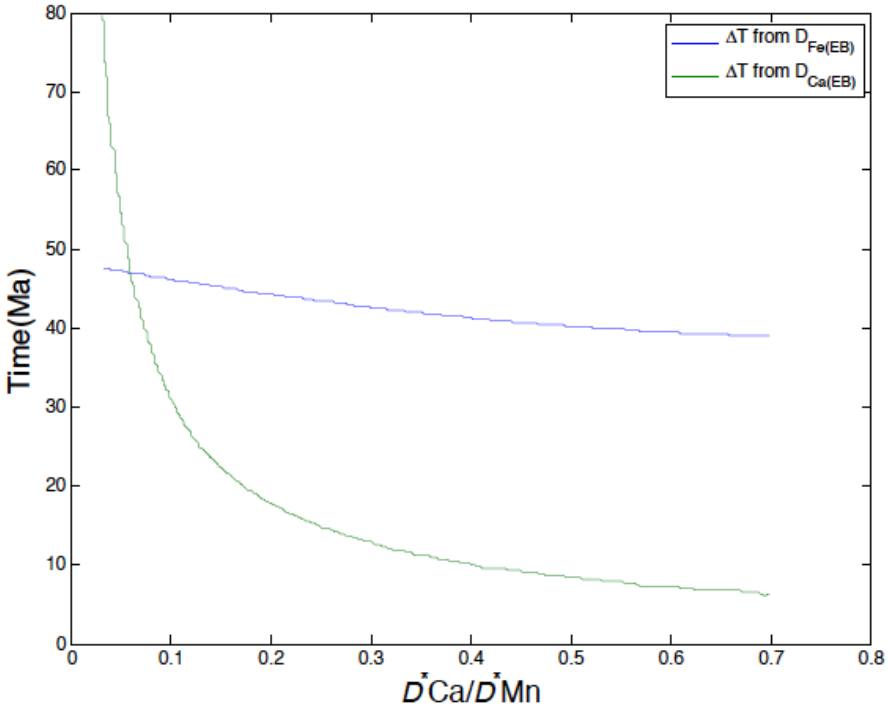

Figure 3.2: Variations in calculated time scales (Δ_t) as functions of $D_{Fe(EB)}$ and $D_{Ca(EB)}$, derived from assumed values of D^*_{Ca}(27).

where D^*_i is the self diffusion coefficient of the component i,n is the dependent component, and δ_{ij} is the Kronecker delta. Ideal values for $D_{Fe(EB)}$ and $D_{Ca(EB)}$ were calculated from low-temperature extrapolations. Due to a lack of experimental data, D^*_{Ca} was treated as an unknown, and varied until the values for $D_{Fe(EB)}$ and $D_{Ca(EB)}$ matched Equations 3.6 and 3.7. Figure 3.2 illustrates convergence of ideal EBDCs for Ca and Fe at a Δt of approximately 47 Ma.

In order to adapt this method for the study of metal alloys, the $\boldsymbol{D}$ matrix should be populated by using the Ziebold-Cooper Procedure, an extension of Darkens equation of multi-component diffusion as follows (29), in lieu of Equation 3.8.

$$D^n_{ik} = \sum_{m-1}^{n-1} D^*_m \delta_{im} - N_i(D^*_m - D^*_n)\frac{N_m}{N_k} g_{mk} \tag{3.9}$$

where i is the number of components, D_m^* is the self-diffusion coefficient, a_i is the activity of the $i-th$ component, and δ_m is the Kronecker delta function.

To illustrate the implications of this solution, this paper examines an alloy with known tracer diffusion coefficeints (D_i^*), and Gibbs free energies. Desestret et al. (30) and Assassa et al. (31) conducted tracer experiments on an austenitic FeCrNi alloy of molar fraction composition 0.196 Cr and 0.1057 Ni at 1100^{o}C and determined that (all values are in m^2s^{-1}):

$$\begin{aligned} D_{Cr}^* &= 1.92 * 10^{-15} \\ D_{Ni}^* &= 7.62 * 10^{-16} \\ D_{Fe}^* &= 1.28 * 10^{-15} \end{aligned} \tag{3.10}$$

Using the Gibbs free energies obtained by Hillert and Waldenstrom (32), and Equation 3.9, the matrix of thermodynamic coefficients is:

$$\begin{bmatrix} g_{CrCr} & g_{CrNi} \\ g_{NiCr} & g_{NiNi} \end{bmatrix} = \begin{bmatrix} +1.177 & -0.321 \\ -0.710 & +1.002 \end{bmatrix} \tag{3.11}$$

For the alloy in question, assuming Cr=1, Ni=2, and Fe=3 (the solvent), the ternary diffusion coefficients are found through the use of Equation 3.12:

$$\begin{aligned} D_{11}^3 &= [D_1^* - N_1(D_1^* - D_3^*)]g_{11} - N_2(D_2^* - D_3^*)g_{21} \\ D_{12}^3 &= [D_1^* - N_1(D_1^* - D_3^*)](N_1/N_2)g_{11} - N_1(D_2^* - D_3^*)g_{22} \\ D_{22}^3 &= [D_2^* - N_2(D_2^* - D_3^*)]g_{22} - N_1(D_1^* - D_3^*)g_{12} \\ D_{21}^3 &= [D_2^* - N_2(D_2^* - D_3^*)](N_2/N_1)g_{11} - N_2(D_1^* - D_3^*)g_{11} \end{aligned} \tag{3.12}$$

Applying the values in Equations 3.10 and 3.11 to Equation 3.12 yields:

$$\begin{bmatrix} D_{11}^3 & D_{12}^3 \\ D_{21}^3 & D_{22}^3 \end{bmatrix} = \begin{bmatrix} +2.07 & -1.31 \\ -0.35 & +0.86 \end{bmatrix} * 10^{-15} m^2 s^{-1} \tag{3.13}$$

For ideal solutions, (where the activity of each atom species is equal to its atom fraction, the atoms species of ideal solutions must be made up of elements that are chemically very similar, if not identical), g_{ik} can be replaced with unity (29). Using the values in the D matrix in Equation 3.13, and assuming it to be constant, the program PROFILER (11) was used to generate diffusion profiles. The simulation was for 3.6x10^{5}s, and exhibited no evidence of uphill diffusion. The initial concentration differences were assumed to be as shown in Figure 3.3.

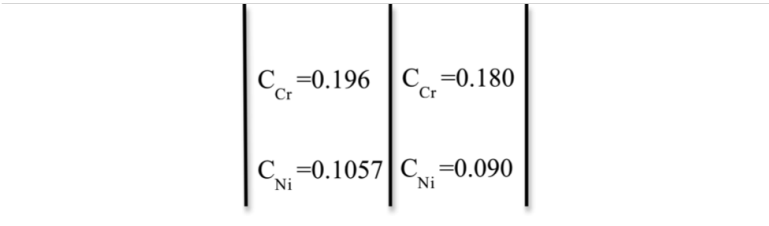

Figure 3.3: Initial concentrations of example diffusion couple.

Given these values for ternary diffusion, one can use an equation similar to Equation 3.6 and select concentration data from the center of the diffusion zone (approx. 2100 nm) to ensure an average. The values were calculated to be:

$$D_{Cr(EB)} = 2.982 * 10^{-15} m^2 s^{-1} \tag{3.14}$$

$$D_{Ni(EB)} = 1.3627 * 10^{-15} m^2 s^{-1} \tag{3.15}$$

To illustrate the effects of time on isothermal diffusion, Figure 3.4 shows the effects of varying the aging time at T_{ch}, the characteristic temperature of diffusion, which is based on the experimental data at 1100^{o}C.

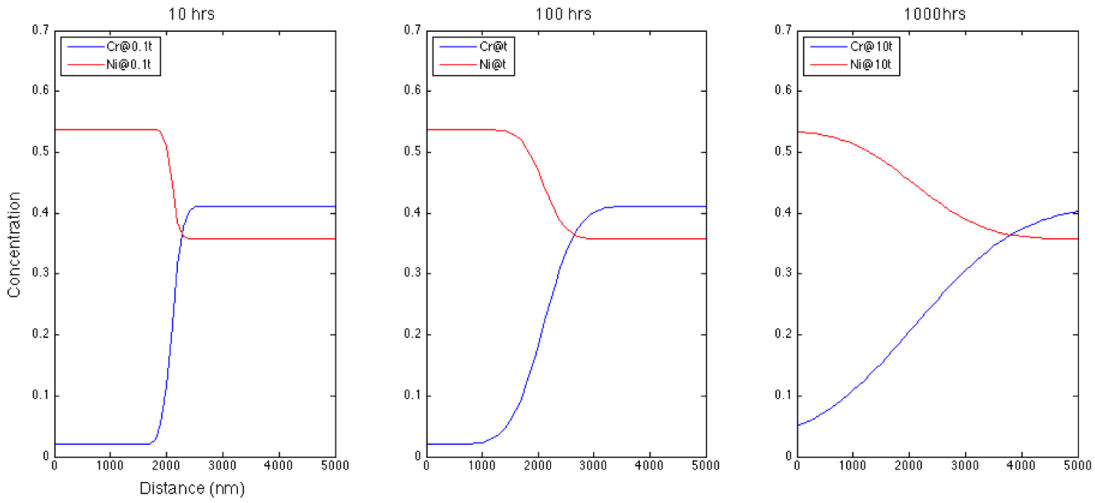

Figure 3.4: Concentration profile at varying times.

The profiles are clearly influenced by the effects of time, and further examination of these profiles in alloys of known composition and age could greatly benefit our ability to determine the age of unknown samples.

3.1.3 Uncertainties

Small errors when calculating T can lead to large errors in calculating D or Δt. In Ganguly's study of garnet, where the activation energy is 60 kJ/mol, an error of $\pm 15°C$ will cause an increase in uncertainty by a factor of 3 (27). The application of these principles to uranium illustrate similar perils, as the activation energy for impurity diffusion in uranium ranges from 52 kJ/mol for Co to 127 kJ/mol for Au (13).

Generally, the higher an atom's activation energy, the more sensitive it is to temperature changes ($D \propto e^{-Q/RT}$). Figure 3.5 illustrates the effects of a variance in temperatures and activation energy on calculated D values. The value for D calculated at 300 K is 3.7532x10^{-29} m^2 s^{-1}, while at 315 K it is 4.24x10^{-28} m^2 s^{-1}.

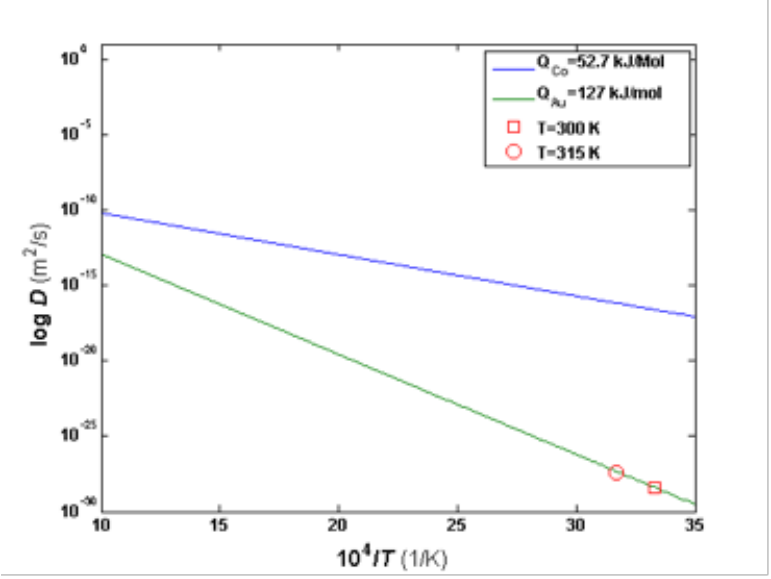

Figure 3.5: The effects of uncertainty in temperature on diffusion coefficients.

The greater the activation energy, the steeper the slope of the line, and the more significant the range of temperatures.

Another potential source of error is the low temperature extrapolation of experimental diffusion data according to Arrhenian relations The lowest experimental temperatures for which data is provided is 683 K, (13) nearly 300 K greater than normal ambient temperatures. Whether or not the diffusion mechanism in uranium changes between 300 and 683 K is outside the scope of this study, but bears further consideration in future experiments. The low temperature extrapolation would lead to an overestimate of the value of Δt.

Chapter 4

Radiolytic Damage

The determination of trace levels of impurities and activation products in found or confiscated nuclear materials can provide information for forensic purposes, such as; the production location, fabrication methodology, and the raw materials employed. Currently, the most well-known tool to document the age of a sample is to calculate the relative concentration of radionuclides linked to one another through radioactive decay (1).

The introduction of vacancies and defects from naturally occurring radiation can alter a material's structure (33)(34). In addition to ionizing α-particles, uranium decays cause thousands of permanently displaced atoms primarily by direct impacts within damage cascades caused by the heavier recoil atoms. Two uranium isotopes

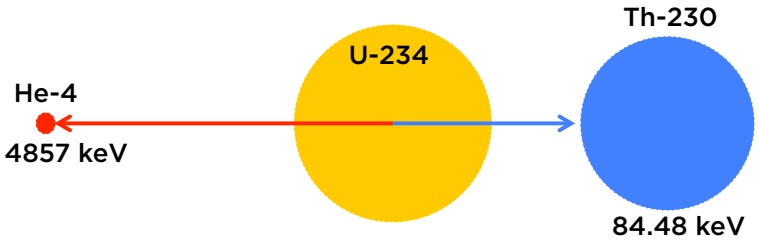

Figure 4.1: Physical representation of ^{234}U decay.

can contribute to significant radiolytic damage in uranium-bearing materials: 1) the naturally occurring ^{234}U isotope and 2) the ^{232}U isotope, which may be present in trace amounts from prior reprocessing and/or re-enrichment activities. The mechanism for radiolytic damage is expected to be dominated by the total α-particle dose that the metal/alloy undergoes (arising from all the isotopes of uranium and their progeny present in the sample).

In metal produced from pristine (i.e., unirradiated stock) uranium, the ^{234}U dominates. In reprocessed uranium components, ^{232}U at concentrations above 3 ng/g-U will contribute. Above 100 ng/g-U, ^{232}U will dominate the damage (35). This is a concern to the forensic utility of this method when considering uranium produced from uranium recovered from spent fuel that has been reprocessed and re-enriched, which will concentrate the ^{232}U preferentially. Therefore, the radiolytic method must always be supported with radiochemical and isotopic composition data on a questioned article.

Uranium-232 is typically formed during the irradiation of uranium and thorium samples (Equations 4.1, 4.2)(36), and is a characteristic of previous neutron irradiation and reprocessing of illicit uranium-based nuclear materials (37).

$$^{237}Np(n,2n)^{236}Np \rightarrow \beta + ^{236}\,Pu \rightarrow \alpha + ^{232}\,U \tag{4.1}$$

$$^{234}U(n,2n)^{233}U(n,2n)^{232}U \tag{4.2}$$

4.1 Kinetics

Uranium-232 is typically measured using a combination of gamma and alpha spectroscopy, due to spectral overlap with ^{232}Th and the tailing from ^{233}U. Its relatively short half-life, as compared to other uranium isotopes, means that its daughters can be found in larger quantities in samples (36). Of significance to the

study of defect and impurity migration is that ^{232}U decays by emitting α-particles with energies over 5.3 MeV and has a half-life of 68.9 years. This particle is significantly higher in energy than any other α-particle emitted by the decay of uranium isotopes and this is easily quantified (36). In addition to self-heating, these interactions produce large number of electron-hole pairs and can lead to the rupture of covalent and ionic bonds, enhanced self-diffusion and defect diffusion.

In an α-decay event, the α-particle and the α-recoil particle are released in opposite directions and produce distinctly different damage regions (see Figure 4.1). Based on full cascade Monte Carlo calculations using the SRIM-2008 code, and assumed displacement energy (E_d=40 eV), the average number of displacements created by the 4.8 MeV α-particle and the 88 keV ^{230}Th released in the decay of ^{234}U have been determined to be approximately 175 and 1150 respectively, in ^{238}U. Many of these defects recombine within picoseconds of the initial damage event, and thus the number of defects surviving the cascade will be significantly smaller. These results are heavily dependent upon the assumed displacement energy (E_d), the minimum kinetic energy necessary to displace an atom from its normal site. We used the currently accepted value (40 eV) for uranium in these simulations (38). Further experimental results are needed to confirm or deny these results in order to accurately model the relationship between time and the surviving number of defects in uranium and other metals of concern.

Ballistic processes cause direct atomic displacements through scattering collisions and cause rearrangement of the atomic structure. The α-particles lose energy predominately through ionization between 7.5-8.1 μm, but undergo elastic collisions in sufficient numbers to create hundreds of atomic displacements and subsequent Frenkel pairs, the largest numbers of which are at the end of the α-particle's range. The more massive, but less energetic recoil ^{230}Th accounts for the majority of the total displacements produced by these ballistic processes. The recoil will lose 80% or more of its energy in elastic collisions over a considerably shorter range (8-12 nm) and produce more energetic recoils, generating more elastic collisions. High energies

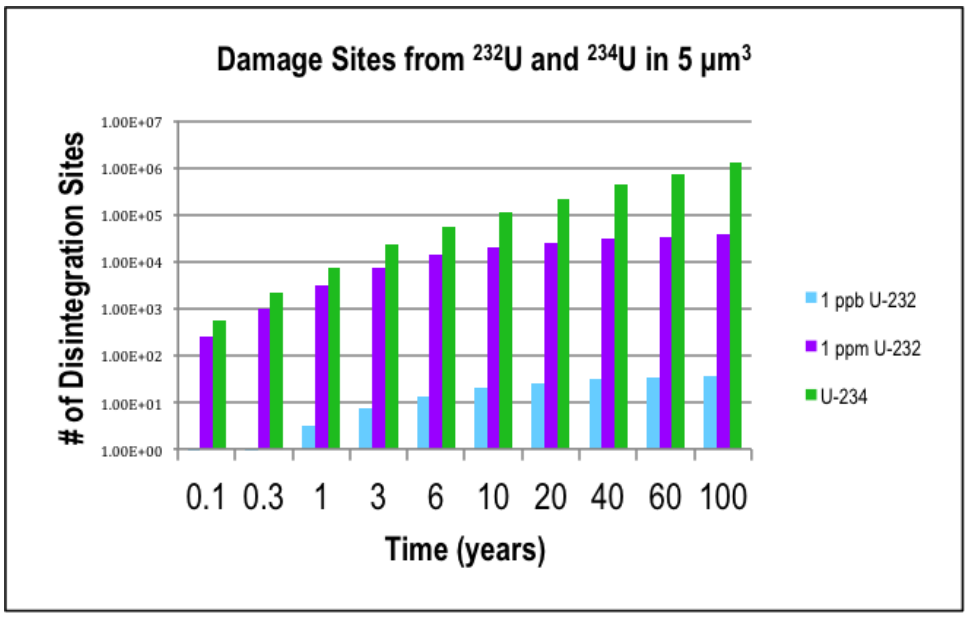

Figure 4.2: Comparison between ^{234}U and ^{232}U-specific damage sites (35).

deposited over the initial portion of the cascade may lead to local melting in the cascade or more atomic rearrangements and relaxations, such that the number of disordered atoms will exceed the number of displaced atoms from ballistic events (39).

4.2 Effects of Damage Accumulation

Figure 4.2 illustrates the comparison between ^{234}U and ^{232}U-specific damage sites, corresponding to the addition of ^{232}U to the U900 standard at. concentrations of 1 ppm and 1 ppb within a 5μm volume. The OrigenARP module in SCALE 6.1 was used to determine the number of progeny isotopes and the number of α-disintegrations as a function of time. As seen in Figure 4.2 the ^{234}U decay chain dominates the number of damage sites within uranium metal.

Self-radiation creates vacancies, interstitials and helium atoms, and their numbers increase with each decay event. These defects are mobile and migrate throughout the

metals to either recombine or be absorbed at defect sinks. This motion is the driving force for processes such as defect clustering, bubble formation, and amorphization (34).

The effects of α-decay damage as applicable to the storage of waste have been thoroughly examined (33)(34)(39)(40)(41). Over the time scales of concern to nuclear waste storage, (10 to 10^6 years), and at low temperatures, α-decay and ion-irradiation damage result in a the transition from a crystalline to an aperiodic, or amorphous state in most of the crystalline ceramics that have been investigated (34). Similarly, ion irradiation of crystalline metallic alloys can also cause amorphization, the loss of long-range order, or a change to a different crystal structure. Irradiation-induced amorphization can occur heterogeneously in the cores of the displacement cascades or homogeneously as the result of the accumulation of point defects and small defect clusters. The material undergoes a phase transition to an amorphous state and neither long range nor short-range order of the atoms can be found.

Heavy-ion irradiation in conjunction with α-particle irradiation can create displacement cascades where the effective displacement rate is comparable to the displacement rate caused by long-term exposure to α-decay, such that the damage processes outweigh the recovery rate. Several models currently exist to determine the amorphous fraction (f_a) based on dose (41). The simplest models do not take into account simultaneous recovery processes and are generally valid only for irradiation at low temperatures. Amorphization depends on the relative magnitude of production and recovery processes under any given irradiation condition, and recovery can be thermal or irradiation driven (40).

Swelling which results from radiation-induced damage, can be directly linked to the cumulative dose in specimens as a function of time. In 1993, Weber (40) explored the changes in unit cell parameters as a function of dose in complex silicate structures and observed anisotropic changes in the cell parameters of a Cm-doped $Ca_2Nd_8(SiO_4)_6O_2$. Measurements showed $\Delta a/a_o$ measuring nearly twice $\Delta c/c_o$. However, these lattice expansions were a result of changes in oxygen-oxygen distances

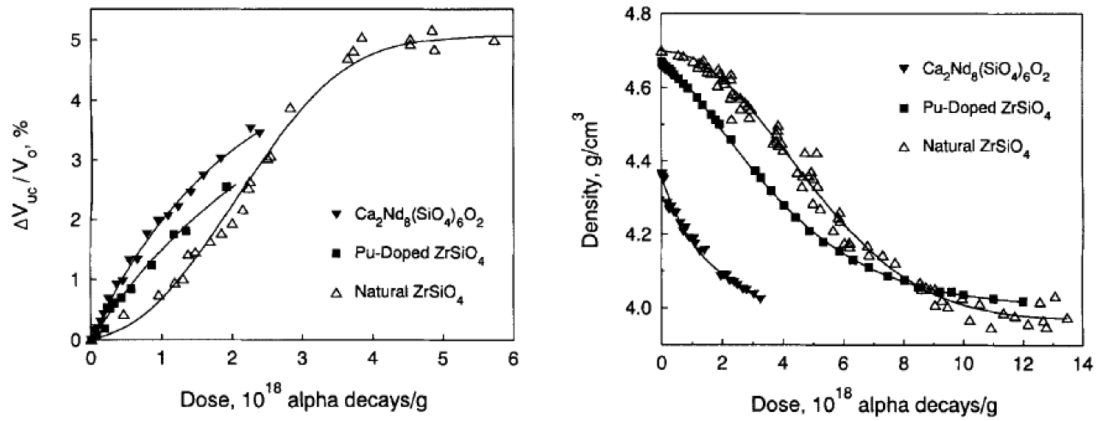

(a) (b)

Figure 4.3: (a)Unit cell volume expansions, (b) Density changes in Cm-doped $Ca_2Nd_8(SiO_4)_6O_2$, Pu-doped $ZrSiO_4$, and natural $ZrSiO_4$ (40).

and cation separations. The changes in unit cell volume $\Delta V_{uc}/V_0$ are predicted by the following equation:

$$\Delta V_{uc}/V_0 = A_{uc}[1 - exp[-(B_{uc}D)]] \tag{4.3}$$

where A_{uc} is the unit cell volume change at saturation and B_{uc} is a rate constant (per unit dose) for the simultaneous recombination of Frenkel defects during irradiation. Another approach based on cumulative dose is the macroscopic swelling, or decrease in volume of the irradiated materials.

$$\Delta V_m/V_0 = -(\Delta\rho/\rho_0)/(1 + \Delta\rho/\rho_0) \tag{4.4}$$

Examples of changes in unit cell volume and density can be found in Figure 4.3a and b, respectively. Experimental results indicated that the volume of disordered material which survives each cascade in $ZrSiO_4$ to be one-half to three-fourths the calculated cascade volume.

In order to accurately determine the time since forming, it will be necessary to determine the relationship between the dose and the time that the sample has been exposed to self-irradiation. Current data has focused on times necessary for spent fuel storage, whereas for forensic purposes the damage data would need to be accurately modeled for a period of 0-60 years. Figure 4.4 illustrates the visualization of damage caused by 10 years of storage in an ideal TEM specimen, where the ideal specimen is defined as 50nm x 10μm x 10μm. A specimen of uranium metal with isotopic content similar to U900 would exhibit 56000 damage sites in a 5 μm^3 specimen after aging (35).

4.3 Radiolytic Damage as a Chronometric Tool

For over 50 years, the tracks created by the spontaneous fission of ^{238}U (see Figure 4.5) have been used to reconstruct low-temperature thermal history of rocks on geological time scales (42)(43)(44). The tracks are created by the displacement of atoms in the host lattice through collisions with fission products. Radiometric age is determined by three parameters, the numbers of parent and daughter nuclides in a material, the decay constant for the parent nuclide (42).

4.3.1 Fission Track Dating

In the Fission Track (FT) method, the relevant parameters are: ^{238}N, the number of ^{238}U per volume, N_s, the number of spontaneous fission tracks per unit volume, and λ_F, the decay constant for spontaneous fission. Because ^{238}U α-decays 2x10^6 more frequently than it spontaneously fissions, that decay constant must also be considered(λ_D) (42). Thus, the number of spontaneous fission tracks as a function of time is given by:

$$N_s = \frac{\lambda_F}{\lambda_D}^{238} N\{exp(\lambda_D t) - 1\} \tag{4.5}$$

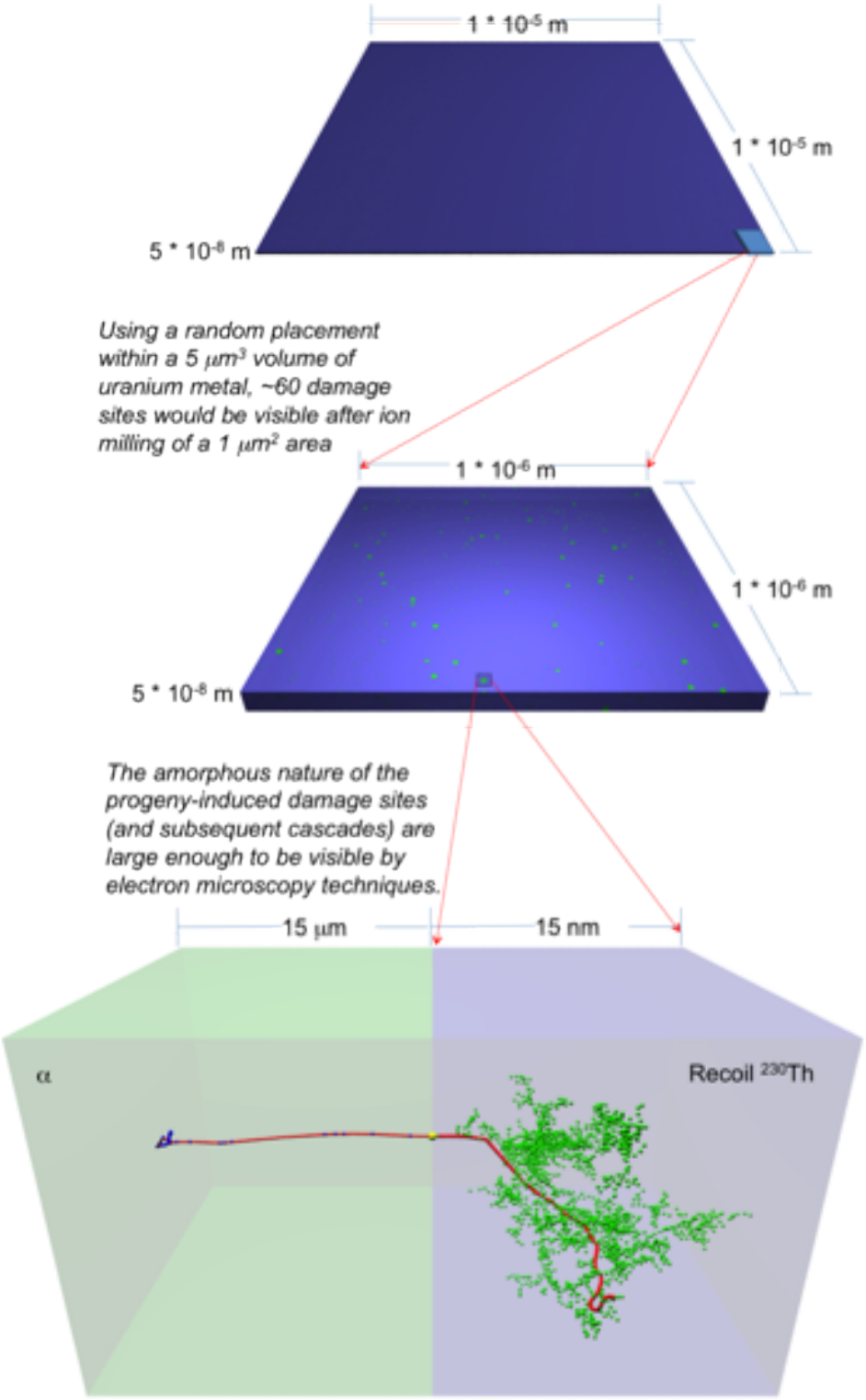

Figure 4.4: SRIM Trajectories (red) for the 4.8 MeV α-particle (left) and recoil ^{230}Th (right) in uranium metal corresponding to the decay of the ^{234}U isotope. [Note the 3-order of magnitude difference in the scale of the two trajectories] (35).

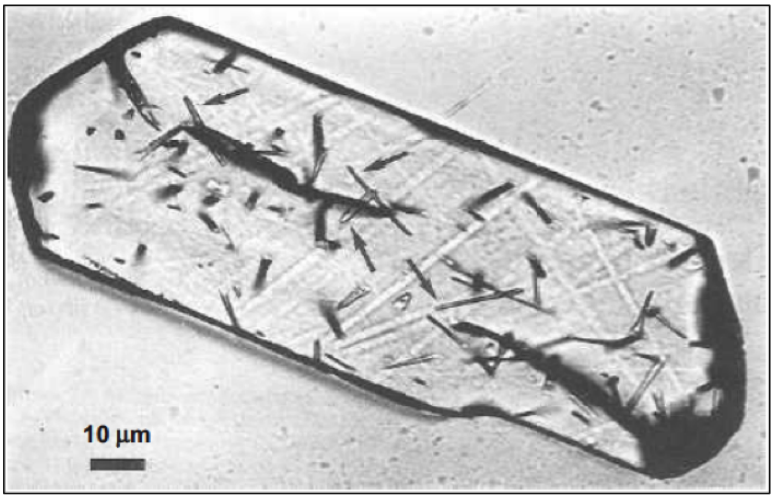

Figure 4.5: Spontaneous tracks on a polished internal surface of 33 Ma apatite crystal (42).

In order to measure the number of ^{238}U atoms present, the fission of ^{235}U is artificially induced through thermal neutron irradiation. The number of induced fission tracks per unit volume N_i is given by:

$$N_i =^{235} N\sigma_F\Phi \tag{4.6}$$

where ^{235}N is the number of ^{235}U per unit volume, σ_F is the cross section for induced nuclear fission of ^{235}U by thermal neutrons (580 barns), and Φ is the thermal neutron fluence. Coupling these equations yields:

$$t = \frac{1}{\lambda_D} ln \left\{ 1 + \left(\frac{\lambda_D}{\lambda_F} \right) \left(\frac{N_S}{N_I} \right) I\sigma_F\Phi \right\} \tag{4.7}$$

where I is the isotopic abundance of U,($^{235}N/^{238}N$). Only tracks intersecting the prepared surface are observable under optical microscope, thus:

$$t = \frac{1}{\lambda_D} ln \left\{ 1 + \left(\frac{\lambda_D}{\lambda_F} \right) \left(\frac{\rho_S}{\rho_I} \right) QGI\sigma_F\Phi \right\} \tag{4.8}$$

where ρ_S is the surface density of etched spontaneous fission tracks, ρ_I is the surface density of etched induced fission tracks, Q is the integrated factor of registration and observation efficiency of fission tracks, and G is the integrated geometry factor of etched surface. To determine the age of an unknown sample, three measurements are taken: ρ_S,ρ_I, and ρ_D. To determine those densities, the number of etched tracks that intersect the surface within a known area are counted using an optical microscope at magnifications of at least 1000x (42). Typically, between 10 and 30 single-grain ages are determined to ensure an accurate FT analysis. If the grains within the sample have a common age, the variation in single grain ages is governed only by the Poissonian statistics concerned with the determination of ρ_S, ρ_I, and ρ_D.

4.3.2 Attempts at α-recoil Track (α-RT) Dating

In 1967, Huang and Walker (45) first proposed using the density of damage sites created by the α-decay of uranium isotopes as an additional method to date samples. They examined etched samples of mica under normal bright field illumination, and subsequently in phase contrast. Figure 4.6 provides an example of their samples.

They asserted that the large number of visible damage cites were caused by the heavy recoil particles during uranium and thorium decays, and not the ejected α-particle for these four reasons:

1. The ratio of smaller tracks to fission tracks is approximately constant in samples with very different uranium concentrations

2. The depth of the shallow pits, or track lengths, inferred on the basis of the α-recoil hypothesis agrees with the experimental value obtained by electron microscopy

3. The measured length is also compatible with the theoretical range of α-recoils

4. The α-emitter ^{228}Th, placed next to annealed mica produces new shallow pits with the proper frequency

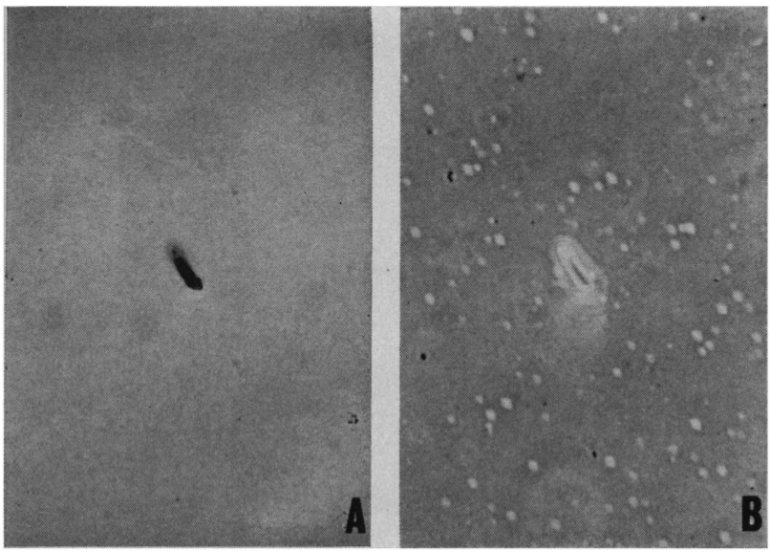

Figure 4.6: Comparison between fission tracks and α-decay cites.(45)

They proposed the following equation to predict the density of α-recoil tracks:

$$\rho_\alpha = N_0 C_U \lambda_\alpha(U) T R_\alpha + N_0 C_{Th} \lambda_\alpha(Th) T R_\alpha \tag{4.9}$$

where $\lambda_\alpha(U)$ is the α-decay constant, C_U is the concentration of U/Th, R_α is the total etchable range of the two fragments emitted from a decay, T is the time and N_0 is the number of atoms per unit volume.

Huang and Walker conducted two experiments. In the first, an annealed sample of mica was placed in contact with a uranium foil for 12 days. In the second experiment, solutions containing various concentrations of ^{228}Th were evaporated on anneal mica for 20 hours and subsequently rinsed and etched. Annealing at 600^{o}C had reduced the α-recoil density to approximately 200 cm^{-2}. The ^{228}Th experiment yielded shallow pits, identical to those found in the fossil mica, however none were observed in the U-foil experiment.

In 1981, Hashemi-Nezhad and Durrani (46) re-examined Huang's work, asserted that observed tracks we indeed from single recoils, outlined obstacles preventing the

use of α-recoil track dating, and proposed potential advantages; should the obstacles be overcome. They proposed using Fleischer's (47) equation for the decay density as follows:

$$\rho_\alpha = \sum_i [exp(\lambda_{\alpha i} T) - 1](N_v C_i R_{\alpha i} \eta_i) \tag{4.10}$$

where $\lambda_{\alpha i}$ is the α-decay constant of the i-th element concerned, N_v is the number of atoms per unit volume of the sample, C_i is the fraction of atoms that are element i, $R_{\alpha i}$ is the range of α-RT resulting from the α-decay of series i, and η_i is the etching efficiency fro α-RTs due to element i. This equation addresses the following shortcomings of Equation 4.9: it allows for variations in the etching efficiency for α-RTs and it allows for different ranges for each α-decay. However, it fails to address the following possible sources of error: it does not account for the effects of etching time and ignores the possibility of the migration of daughter atoms. Hashemi-Nezhad and Durrani (46) also modified Equation 4.10 for comparison between reference samples of a known age, and an object of similar composition, but an unknown age from the equation:

$$\frac{\rho_x(t)}{\rho_s(t)} = \frac{\sum_i [exp(\lambda_{\alpha i} T) - 1] C_{ix}}{\sum_i [exp(\lambda_{\alpha i} T') - 1] C_{is}} \tag{4.11}$$

where the subscripts x and s denote the unknown and standard samples, respectively, and t denotes etching time. This approach required identical etching times, and etching efficiencies. It also must account for the possibility of losses due to annealing, or that the losses are similar among specimens. At the time of publication, Hashemi-Nezhad and Durrani concluded that they possessed insufficient knowledge of the behavior of α-decay in solids to made α-RT dating a viable method.

4.3.3 SRIM Calculations and Range

In an effort to improve the accuracy of the methods described in the preceding sections, Full Cascade damage simulations in SRIM-2008 calculated the range of

the recoil nuclei from the long-lived daughter isotopes created by the decay of the Certified Reference Materials (CRMs) in Table 4.1.

Table 4.1: Isotopic Contents of Various CRMs (w%)(35).

CRM	^{234}U	^{235}U	^{236}U	^{238}U
U0002	0.00016	0.01733	0.00001	99.9825
U005-A	0.0034	0.5	0.00117	99.4955
129-A	0.0052075	0.71183	0.0000096	99.28295
U015	0.00836	1.5132	0.0136	98.462
U045	0.03809	4.4599	0.027483	95.4746
U200	0.1229	19.811	0.2103	79.856
U350	0.2467	34.903	0.1667	64.684
U750	0.588	75.129	0.2502	24.033
U900	0.7735	90.098	0.3337	8.795
U930	1.0759	93.276	0.2034	5.445

The OrigenARP module in SCALE 6.1 calculated the concentration of daughters for the decay of U0002 and U930 at times out to 100 years, these values were then used to compute the necessary parameters to solve Equation 4.10. The range of all the daughter recoils were found through full damage cascade simulations in SRIM-2008. The density of the CRMs varied from 19.1 to 19.05 g/cm^3 as the concentration of ^{238}U decreased. The differences in density resulted in a $\pm 5\mathring{A}$ difference in ranges for the most massive and energetic particles, such that all damage sites would look essentially identical in both/all CRMs under scanning electron microscopy. The daughters have masses from 206-234 amu and energies ranging from 72-147 keV. The ranges and energies of the recoils in U930 can be found in Table 4.2

Figure 4.7(a) shows the density of α-damage sites in both U0002 and U930. The solid line represents density calculated using only the U/Th isotopic data, as proposed by Hashemi-Nezhad and Durrani. By incorporating the decay of other longer-lived daughter isotopes, ^{231}Pa, ^{226}Ra, ^{210}Po, and ^{210}Bi, the damage density greatly increases at times beyond 10 years.

Table 4.2: Range of daughter nuclei produced by α-decay in U930.

Recoil	Energy	Range(Å)
^{234}Th	73 keV	97±53
^{232}Th	79 keV	104±56
^{231}Th	81 keV	105±56
^{230}Th	85 keV	106±59
^{228}Ra	72 keV	97±55
^{227}Ac	90 keV	109±58
^{227}Ra	74 keV	97±53
^{226}Ra	84 keV	107±57
^{224}Ra	99 keV	119±64
^{223}Ra	110 keV	130±68
^{222}Rn	88 keV	106±56
^{220}Rn	105 keV	125±67
^{219}Rn	109 keV	129±68
^{218}Po	103 keV	126±67
^{215}Po	114 keV	137±70
^{214}Pb	129 keV	147±72
^{211}Pb	143 keV	147±75
^{208}Pb	119 keV	139±71
^{207}Pb	147 keV	157±77
^{207}Tl	130 keV	152±76
^{206}Pb	105 keV	130±68
^{206}Tl	98 keV	126±67

Currently the issues with this modeling approach are illustrated in Figure 4.7(b): (i) incorporating the decay of ^{231}Th causes a prompt increase to a damage density of nearly 10^{100} damage sites per nm^3, and (ii) the decay of ^{227}Th dominates, creating a linear increase in damage beyond 2.5 years. As a forensic tool, the potential for spoofing exists. Ion beam irradiation could increase the damage density considerably, which further reinforces the need to use this method in conjunction with a suite of other chronometric tools to ensure accuracy.

The models proposed in the preceding sections do not account for the annealing of α-recoil tracks, and ignore the defects caused by the decay of the short-lived

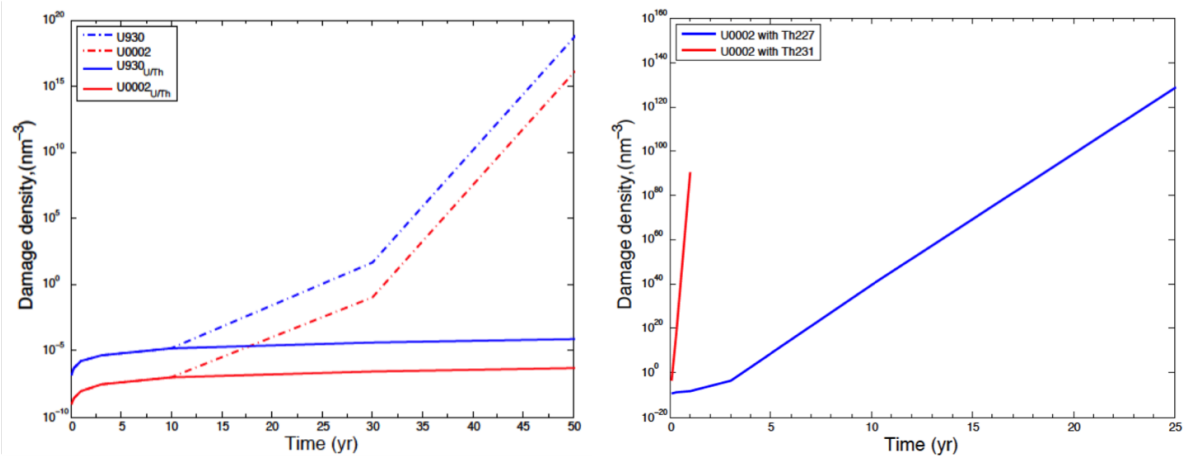

Figure 4.7: Modeled density of α-recoil tracks: (a) including long-lived daughters, (b) incorporating the decay of ^{227}Th and ^{231}Th.

daughters. Hashemi-Nezhad and Durrani's approach assumes that the short-lived daughters caused damage thousands/millions of years ago, when the samples were at elevated geologic temperatures, and thus subject to annealing. Further experimental data is required to describe the behavior of these damage regions and to quantify and characterize them in samples of known ages. Researchers must also explore the effects of temperature on annealing and track length, as heat tends to heal radiation damage tracks.

4.4 (U-Th)He Dating

Helium atoms are created when α-particles capture two electrons and must: (i) be accommodated interstitially, (ii) be trapped at internal defects, (iii) aggregate to form bubbles, or (iv) be released at the surface.

The effects of the helium atoms generated through α-decay have been thoroughly studied in metals (48)(49)(50)(51). Helium atoms can bind with interstitials and can prevent either atom from occupying a position in the lattice, and cause an

increase in the number of vacancies. A helium atom at an interstitial position can migrate quickly through the lattice until it finds a sink such as a vacant site, grain boundary, dislocation or the surface. At low temperatures, it is well established that this diffusion method dominates (49). Also, the presence of dislocations and grain boundaries affect He behavior in the sense that these complex defects represent sinks as well as preferential diffusion paths depending on their structures (51).

Radiogenic helium has long been used as a low temperature chronometer, and to provide information about the time-temperature evolution of geologic samples (52). However, as early as 1910 it was known that the ages obtained from this method were at best "minimum values, because He leaks out from the mineral, to what extent it is impossible to say"(53). Most dating procedures involve measuring the parent and daughter nuclides on the same aliquots, due to the potential for varying concentrations among crystals. Presently, reasonably precise ages using routine methods require ^{4}He contents as high as 0.3 fmol (in a typical zircon crystal, this is 20,000 yrs of ingrowth) (54). Fortunately for forensic applications, the temperature range best suited for this method of thermochronometry in minerals is between surface temperatures and 130^{o}C.

Applying our knowledge of (U-Th)/He cooling ages in the geologic samples to forensic problems requires that work validated in laboratories to be extrapolated to the conditions of interest, i.e., storage at ambient temperatures for periods of days to decades. Naturally occurring ^{4}He generally does not reside in uniform concentration distributions, and thus experiments alone cannot determine diffusion coefficients, nor is it present in sufficient quantities, particularly in materials with low levels of radiation damage (55).

In 2006, Shuster *et al.* (56) examined the influence of natural radiation damage on He diffusion kinetics in apatite. They presented several challenges when measuring ^{4}He as a proxy for U/Th decay-induced damage. For the following reasons, assuming that the levels of ^{4}He are proportional to the level of damage is an oversimplification: (i) ^{4}He can be lost by diffusion, (ii) the extent of damage is sensitive to temperature,

and (iii) damage can anneal. At temperatures above T_c, the closure temperature, damage can/will accumulate. Also of significance, radiation damage at typical levels impedes He mobility by creating traps from which the He atoms must escape before they can diffuse through undamaged lattices. The threshold for damage accumulation from α-decay is expected to be similar to that of spontaneous fission in apatite (44). Shuster's model predicts that at temperatures suitable for damage accumulation, higher effective uranium concentration (eU) (computed as [U]+0.235x[Th]) will accumulate more damage traps and develop a higher He closure temperature than an specimen with lower eU that accumulates fewer damage traps.

In 2009, Shuster and Farley (55) attempted to confirm and quantify the effects of damage accumulation and annealing on the kinetics of helium diffusion. Ultimately, they determined that the amount of radiolytic damage in apatite crystals strongly influences the kinetics of helium diffusion, and that diffusivity is an evolving function of time governed by both temperature and the eU in a sample. They monitored the diffusion of He in apatite as the amount of damage from artificial irradiation increased and when the samples were subsequently annealed. The most significant contributors to the damage environment are the recoil nuclei identified in the preceding section. These displacements can either aide or inhibit the diffusion of He. Their method was two-fold; first they used neutron irradiation to simulate the effects of natural radiation damage, and subsequently they exposed their apatite samples to temperatures at which annealing is known to occur.

There are significant shortcomings to measuring He as a proxy for radiation damage: damage may accumulate at temperatures at which He is lost from the crystal, also damage may anneal at a rate that differs from the rate at which He is lost. In an effort to more accurately use He as a proxy for radiation damage, Shuster and Farley adopted the term *effective spntaneous fission-track density* ($e\rho_s$) which is a measure of radiation damage that incorporates contributions from U and Th decay in proportion to α activity. Spontaneous fission track density (ρ_s) is the number density of fission tracks observed on a surface after etching.

Ultimately, the radiation damage accumulation and annealing model (RDAAM) improved the ability to track the evolution and retentivity of He in apatite through the use of effective fission track density rather than He concentrations, as a proxy for the volume fraction of radiation damage.

4.4.1 Summary

Alpha-recoil track dating could be used in a manner analogous to FT dating with the following advantages; because of the increased frequency of α-decay versus spontaneous fission, the increased density of damage sites could allow dating of much younger samples. Additionally, increased densities could enable dating of very small sample crystals. It remains to be seen whether α-recoil tracks can be observed in metallic samples, and a feasible and efficient method for sample preparation is needed. A more comprehensive understanding of the model of helium diffusion in materials of interest is needed in order to accurately interpret the impacts of He diffusion on chronometric data.

Chapter 5

Conclusions

There is significant evidence to support the use of diffusion driven processes to determine the age of a metallic sample. Models describing discontinuous precipitation in both binary alloys and multicomponent systems are decades old. They illustrate conclusively (21)(25) that the aging time of a sample can be predicted based on the amount of precipitate present and an accurate thermal history of the sample. Additionally, this paper explored the use of concentration profiles and the solution to a system of diffusion equations to determine diffusion times (27). With knowledge of thermal histories and adequate data on relevant diffusion coefficients, one can determine the time period over which the diffusion occurred. These sample calculations must be applied to several impurities/precipitates in the future, such that the age is determined by the solution to a system of equations. This paper also identified methods for using the density of damage sites caused by alpha-decay as a chronometer (45)(46). Previously these methods have only been applied to geologic samples. Several shortcomings in current modeling methods exist. There are no models to accurately describe the damage caused by the decay of short-lived daughters of uranium in a sample of uranium metal. Additionally, the temperature at which these defects self-anneal is unknown.

The ability to validate these methods as a useful chronometer depends on several factors. For the diffusion driven processes, we must accurately measure concentrations and diffusion coefficients in materials with much different thermal histories than previously studied, with sufficient accuracy. In the case of radiolytic damage; we must first confirm that alpha-damage sites can be observed in uranium metal samples at ambient temperatures and attempt to quantify this damage in samples of known ages. Provided experimental work is performed with sufficient precision to measure the various physical parameters discussed in this theoretical framework, this work has shown that these complementary methods can provide a chronometric measure of time since a uranium metal object was cast or formed.

Chapter 6

Future Research

In order to validate the approaches suggested in the preceding sections, there is a need for significant experimental work. Efforts should be made to measure chronometric factors in both metallic samples as well as uranium. Materials of known composition and provenance must be aged artificially by heating in order to create control samples. The key challenge needed to demonstrate feasibility is the ability to measure enough impurities and their spatial distributions such that the family of diffusion equations describing their evolution resolves to a narrow time band for the time of forming the microstructure. A significant challenge is the lack of consistent diffusion data at ambient temperatures, and the potential that the phase changes of interest do not occur at reasonable times at these temperatures. This analysis will focus on time-dependent processes such as diffusion of trace and impurity elements, discontinuous precipitation, and conversion of metastable phases. Both binary and multi-component alloys must be artificially aged in order to measure both discontinuous precipitation and impurity concentration profiles.

The second method, based on the number of damage sites caused by α-decay during the self-irradiation of uranium metal is also under consideration. In order to validate the radiolytic damage assertions, samples of a known age and isotopic composition must be prepared for SEM/TEM analysis in order to measure

the necessary parameters, etching efficiency, concentrations and to identify and characterize damaged regions. Further simulations are required to model the long-term behavior of the damage in order to accurately predict the number of surviving damage sites and their appearance. Molecular dynamics simulations could further examine the effects of energetic α-recoil events in relevant materials. Researchers must also examine and attempt to quantify the effects of temperature on annealing and track length.

Bibliography

[1] K. Moody, I. Hutcheon, and P. Grant, *Nuclear Forensic Analysis*. Boca Raton, FL: CRC Press, 2005.

[2] P. Grant, K. Moody, I. Hutcheon, D. Phinney, R. Whipple, J. Haas, A. Alcaraz, J. Andrews, G. L. Klunder, R. E. Russo, T. E. Fickies, G. E. Pelkey, B. D. Andresen, D. A. Kruchten, and S. Cantlin, "Nuclear forensics in law enforcement applications," *Journal of Radioanalytical Nuclear Chemistry*, vol. 235, pp. 129–132, 1998.

[3] M. Wallenius, K. Mayer, and I. Ray, "Nuclear forensic investigations: Two case studies," *Forensic Sci. Int.*, vol. 156, pp. 55–62, January 2006.

[4] R. Wanhill, "Brittle archaeological silver: a fracture mechanisms and mechanics assessment," *Archaeometry*, no. 45, pp. 625–636, Feb. 2003.

[5] R. Wanhill and J. Northover, "Microstructurally-induced embrittlement of archaeological silver," *NLR Technical Publication, National Aerospace Laboratory NLR, Amsterdam*, no. NLRTP-2001-032, 2001.

[6] I. Ravich, "Annealing of brittle archaeological silver: microstructural and technological study," *In 10th Triennial Meeting of the International Council of Museums Committee for Conservation,Preprints of the Seminar: August 22/27*, vol. II, pp. 792–5, 1993.

[7] R. J. H. Wanhill, "Embrittlement of ancient silver," *Journal of Failure Analysis and Prevention*, vol. 5, no. 1, pp. 41–54, Feb. 2005.

[8] F. Schweizer and P. Meyers, "A new approach to the authenticity of ancient silver objects; the discontinuous precipitation of copper from a silver-copper alloy," *Proceedings of the 18th International Symposium on Archaeometry andArchaeological Prospection, Bonn*, pp. 287–298, 1979.

[9] R. Wanhill, J. Northover, and T. Hattenberg, "On the significance of discontinuous precipitation of copper in ancient silver," *NLR Technical*

Publication, National Aerospace Laboratory NLR, Amsterdam, no. NLRTP-2003-628, 2003.

[10] I. Manna, S. Pabi, and W. Gust, "Discontinuous reactions in solids," *International Materials Reviews*, vol. 46, no. 2, pp. 53–91, 2008.

[11] M. Glicksman, *Diffusion in Solids: Field Theory, Solid-State Principles, and Applications*. New York, NY: John Wiley Sons, Inc., 2002.

[12] J. Brady, *Diffusion Data for Silicate Minerals, Glasses, and Liquids, in Mineral Physics Crystallography: A Handbook of Physical Constants*. Washington, D. C.: American Geophysical Union, 2013.

[13] G. Neumann, *Pergamon Materials Series, Volume 14: Self-diffusion and Impurity Diffusion in Pure Metal: Handbook of Experimental Data*. Pergamon, 2013.

[14] J. Ganguly, "Diffusion kinetics in minerals: Principles and applications to tectono-metamorphic processes," *EMU Notes in Mineralogy*, vol. 4, pp. 271–309, 2002.

[15] B. Tougas, C. Blais, F. Chagnon, and S. Pelletier, "Characterization of Nickel Diffusion and its Effect on the Microstructure of Nickel PM Steels," *Metallurgical and Materials Transactions A*, vol. 44, pp. 754–765, 2012.

[16] P. Zieba and W. Gust, "Analytical electron microscopy of discontinuous solid state reactions," *International Materials Reviews*, vol. 43, no. 2, p. 85, 1998.

[17] Zieba and Gust, "Local characterization of the diffusion process during discontinuous phase transformations," *Proceedings of the International Conference on Solid-Solid Phase Transformations 99*, pp. 489–492, 1990.

[18] P. Zieba, "Diffusion along migrating grain boundaries," *Interface Science*, vol. 11, no. 2, p. 52, 2003.

[19] Z. Wang and T. Konna, "Discontinuous precipitation with metastable phase in a Cu 8.6% Sn alloy," *Philosophical Magazine*, vol. 93, no. 8, pp. 949–974, 2004.

[20] K. Malhotra, "Discontinuous precipitation in aluminum-base zinc alloys," *Metallurgical and Materials Transactions*, vol. 3, p. 1521, 1972.

[21] R. Kossowsky, "Cellular precipitation in Ni-55Cr lamellar eutectic and cast Ni-44Cr alloys," *Metallurgical Transactions*, vol. 1, p. 1625, 1970.

[22] M. L. Saucedo-Munoz, V. M. Lopez-Hirata, and H. J. Dorantes-Rosales, "SEM Analysis of Precipitation Process in Alloys," 2005.

[23] M. Kikuchi, M. Kajihara, and S. Choi, "Cellular precipitation involving both substitutional and interstitial solutes: cellular precipitation of Cr_2N in Cr-Ni austenitic steels," *Materials Science and Engineering: A*, vol. 146, no. 1-2, pp. 131–150, 1991.

[24] E. Contreras-Piedras, R. Esquivel-Gonzalez, V. M. Lopez-Hirata, M. Saucedo-Muñoz, A. M. Paniagua-Mercado, and H. J. Dorantes-Rosales, "Growth kinetics of cellular precipitation in a Mg-9.5 Al-0.5 Zn-0.2Mn (wt.%) alloy," *Materials Science and Engineering: A*, vol. 527, no. 29-30, pp. 7775–7778, 2010.

[25] N. Santhi-Srinivas and V. Kutumbarao, "Growth mechanism for discontinuous precipitation in a multi-component (Fe-Al-Cr-Mn-N) system," *Scripta Materialia*, vol. 51, no. 11, pp. 1105–1109, Nov. 2004.

[26] J. Crank, *The Mathematics of Diffusion*. Oxford: Clarendon Press, 1975.

[27] J. Ganguly, S. Chakraborty, T. Sharp, and D. Rumble, "Constraint on the time scale of biotite-grade metamorphism during acadian orogeny from a natural garnet-garnet diffusion couple," *American Mineralogist*, vol. 81, pp. 1208–1216, 1996.

[28] S. Chakraborty and J. Ganguly, *Diffusion, Atomic Ordering, and Mass Transport: Selected Topics in Geochemistry.* New York, NY: Springer-Verlag, 1991.

[29] M. Malik and D. Bergner, "Methods for determination of effective diffusion coefficients in ternary alloys(ii)," *Cryst. Res. Technol.*, vol. 20, pp. 1629–1633, 1985.

[30] A. Desestret, M. Formet, and P. Guiraldenq, *C.R. Adad. Sci. Paris*, vol. 269, p. 1505, 1969.

[31] W. Assassa and P. Guiraldenq., *Met. Sci*, vol. 6, p. 211, 1977.

[32] M. Hillert and M. Walderstom, *Scand. J. Metallurg*, vol. 3, p. 123, 1978.

[33] R. Ewing, W. Weber, and J. Clinard, "The influence of dipole polarisation on threshold displacement energies in uo2," *Prog. Nucl. Energy*, vol. 29, pp. 63–127, 1995.

[34] W. Weber, "Radiation effects in crystalline ceramics for the immobilization of high-level; nuclear waste and plutonium," *Journal of Materials Research*, vol. 13, pp. 1440–1460, 1998.

[35] T. G. Schaaf and A. Loveless, "Unpublished manuscript," 2013.

[36] M. Coleman, "The analysis of uranium-232: comparison of radiochemical techniques and an improved method by alpha spectrometry," *Journal of Radioanalytical Nuclear Chemistry*, vol. 296, pp. 483–486, 2012.

[37] Z. Varga and G. Suranyi, "Detection of previous neutron irradiation and reprocessing of uranium materials for nuclear forensic purposes," *Applied Radiation and Isotopes*, vol. 67, p. 517, 2009.

[38] C. Bishop, S. Murphy, M. Rushton, and R. Grines, "The influence of dipole polarisation on threshold displacement energies in UO_2," *Nuclear Instruments and Methods in Physics Research B*, vol. 274, pp. 195–199, 2011.

[39] R. Ewing and W. Weber, *Actinide waste forms and radiation effects,The Chemistry of the Actinides and Transactinide Element.* New York: Springer, 2011.

[40] W. Weber, "Alpha-decay-induced amorphization in complex silicate structures," *Journal of the American Ceramic Society*, vol. 76, pp. 1729–1738, 1993.

[41] Weber, "Models and mechanisms of irradiation-induced amorphization in ceramics," *Nuclear Instruments and Methods in Physics Research B*, vol. 166-7, pp. 98–106, 2000.

[42] T. Tagami and P. B. O'Sullivan, "Fundamentals of fission-track thermochronology," *Reviews in Mineralogy and Geochemistry*, vol. 58, pp. 19–47, 2005.

[43] R. L. Fleischer, "Fission tracks in solidsproduction mechanisms and natural origins," *Journal of Materials Sciences*, vol. 39, pp. 3901–3911, 2004.

[44] R. A. Donelick, P. B. O'Sullivan, and R. Ketcham, "Apatite fission-track analysis," *Reviews in Mineralogy and Geochemistry*, vol. 58, pp. 49–94, 2005.

[45] W. Huang and R. Walker, "Fossil alpha-particle recoil tracks: A new method of age determination," *Science*, vol. 155, pp. 1103–1106, 1967.

[46] S. Hashemi-Nezhad and S. Durrani, "Registration of alpha-recoil tracks in mica: the prospects for alpha-recoil dating method," *Nuclear Tracks*, vol. 5, pp. 189–205, 1981.

[47] R. L. Fleischer, P. Price, and R. Walker, *Nuclear Tracks in Solids: Principles and Applications.* Washington, D. C.: University of California Press, Berkley, 1975.

[48] M. Caturla, C. Ortiz, and C. Fu, "Helium and point defect accumulation: (ii) kinetic modelling," *Comptes Rendus Physique*, vol. 9, pp. 401–408, 2008.

[49] H. Lefaix-Jeuland, "Helium behavior in Fe-base materials: thermal desorption and nuclear reaction analyses," *Comptes Rendus Physique*, vol. 9, pp. 401–408, 2008.

[50] M. Caturla and C. Ortiz, "Effect of self-interstitial cluster migration on helium diffusion in iron," *Journal of Nuclear Materials*, vol. 362, pp. 141–145, 2007.

[51] H. Lefaix-Jeuland, S. Moll, T. Jourdan, and F. Legendre, "Effect of grain microstructure on thermal helium desorption from pure iron," *Journal of Nuclear Materials*, vol. 434, pp. 152–157, 2013.

[52] D. Cherniak, E. Watson, and J. Thomas, "Diffusion of helium in zircon and apatite," *Chemical Geology*, 2009.

[53] R. Strutt, "Measurements of the rate at which helium is produced in thorianite and pitchblende, with a minimum estimate of their antiquity," *Proc Royal Society of London*, vol. 83, pp. 379–388, 1910.

[54] P. Reiners, "Zircon (U-Th)/He thermochronometry," *Reviews in Mineralogy Geochemistry*, vol. 58, pp. 151–179, 2005.

[55] D. Shuster and K. Farley, "The influence of artificial radiation damage and thermal annealing on helium diffusion kinetics in apatite," *Geochemica et Cosmochimica Acta*, vol. 73, pp. 183–196, 2000.

[56] D. Shuster, R. Flowers, and K. Farley, "The influence of artificial radiation damage and thermal annealing on helium diffusion kinetics in apatite," *Earth and Planetary Science Letters*, vol. 249, pp. 148–161, 2006.

Vita

Ed Peskie was born and raised in Smock, Pennsylvania. After graduating from high school in 1999, he attended the United States Military Academy, where he majored in mechanical engineering and graduated in 2003. Ed then served as an infantry officer in the United States Army, completing two deployments to Iraq and one to Afghanistan. In 2012 he transitioned to Functional Area 52: Nuclear Counter-proliferation, and upon completion of his graduate degree, he will serve as an instructor in the Department of Physics and Nuclear Engineering at the United States Military Academy.